

Characterization of an Iodine-Based Ionic Liquid Ion Source and Studies on Ion Fragmentation

by

Timothy Peter Fedkiw

Submitted to the Department of Aeronautics and Astronautics
in partial fulfillment of the requirements for the degree of

Master of Science

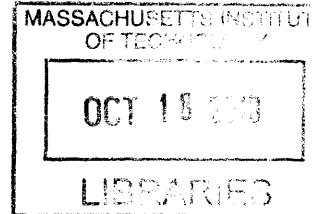
at the

MASSACHUSETTS INSTITUTE OF TECHNOLOGY

August 2010

[September 2010]

© Massachusetts Institute of Technology 2010. All rights reserved.



ARCHIVES

Author
Department of Aeronautics and Astronautics
August 19, 2010

Certified by
Paulo Lozano
Associate Professor
Thesis Supervisor

Accepted by
Eytan H. Modiano
Associate Professor of Aeronautics and Astronautics
Chair, Graduate Program Committee

Characterization of an Iodine-Based Ionic Liquid Ion Source and Studies on Ion Fragmentation

by

Timothy Peter Fedkiw

Submitted to the Department of Aeronautics and Astronautics
on August 19, 2010, in partial fulfillment of the
requirements for the degree of
Master of Science

Abstract

Electrosprays are a well studied source of charged droplets and ions. A specific subclass is the ionic liquid ion source (ILIS), which produce ion beams from the electrostatically stressed meniscus of ionic liquids. ILIS have several applications, two of which include space propulsion and focused ion beam technologies.

An ILIS using the 1-butyl-3-methylimidazolium iodide (BMI-I) is characterized with a focus on those properties that would impact its performance in a focused ion beam (FIB) system. The currents obtained in the negative mode from this ILIS are on the order of 100 nA, and composed of nearly 50% pure iodine ions with the remainder composed of solvated ions. The energy deficit of the ion beam is seen to be on the order of 15 eV, with full width at half maximum of about 12 eV. The angular intensity is estimated to be $0.65 \mu\text{A sr}^{-1}$.

The energy signal from the BMI-I ILIS contained several features that suggested a significant amount of ion fragmentation in the acceleration region. This prompted a secondary study using the ionic liquid 1-methyl-3-methylimidazolium tetrafluoroborate (EMI-BF₄). The amount of fragmentation was seen to be up to 25% of the ion beam. The impact of such fragmentation on the performance of an ILIS thruster is examined. The effects are integrated into the definition of the polydispersive efficiency by characterizing the fragmentation products as two discrete populations of ions and neutrals. This adjusted polydispersive efficiency is seen to be about 88%, about 6% lower than values not taking into account the fragmentation.

Thesis Supervisor: Paulo Lozano

Title: Associate Professor

Acknowledgments

I would like to thank Professor Paulo Lozano for providing me with this opportunity, as well for his support and instruction. His experience and knowledge have been a great help for my work.

I would also like to acknowledge my funding, particularly the Department of Aeronautics and Astronautics and the Department of Defense (DoD) through the National Defense Science Engineering Graduate Fellowship (NDSEG) Program.

Thank you to my fellow graduate students in the Space Propulsion Lab. Your help with experimental equipment and suggestions were invaluable.

Finally I would like to thank my parents, Sharon and Peter. Their support and encouragement of my education throughout my life ensured that I was well prepared to continue to a graduate level.

Contents

| | | |
|----------|--|-----------|
| 1 | Introduction | 13 |
| 1.1 | Electrospray Basics | 13 |
| 1.2 | Ionic Liquids | 14 |
| 1.3 | The Prototypical Ionic Liquid Ion Source | 15 |
| 2 | Electrospray Physics and Applications | 17 |
| 2.1 | Electrospray Physics | 17 |
| 2.1.1 | Taylor Cone Formation | 17 |
| 2.1.2 | Current Emission in the Cone-Jet Regime | 18 |
| 2.1.3 | Field Evaporation of Ions | 19 |
| 2.2 | Electrospray Applications | 20 |
| 2.2.1 | Space Propulsion | 20 |
| 2.2.2 | Focused Ion Beam Applications | 22 |
| 3 | Experimental Techniques | 25 |
| 3.1 | Ion Source | 25 |
| 3.2 | Time of Flight Mass Spectrometry | 27 |
| 3.3 | Retarding Potential Analyzer | 30 |
| 3.4 | Vacuum Chamber and Electronics | 33 |
| 4 | Development of an Iodine ILIS | 35 |
| 4.1 | Motivation | 35 |
| 4.2 | Beam Characterization | 36 |

| | | |
|----------|--|-----------|
| 4.2.1 | Beam Composition | 37 |
| 4.2.2 | Energy distribution | 39 |
| 4.3 | Estimated Performance in a FIB Column | 40 |
| 5 | Full Beam Measurements | 45 |
| 5.1 | Full Beam Time of Flight | 45 |
| 5.2 | Full Beam Retarding Potential Analyzer | 50 |
| 6 | Ion Fragmentation | 57 |
| 6.1 | Signs of Fragmented Ions | 57 |
| 6.2 | Causes | 59 |
| 6.2.1 | Collisions | 59 |
| 6.2.2 | Internal Energy | 61 |
| 6.3 | Effects of Ion Fragmentation | 61 |
| 6.3.1 | Performance of an ILIS Based Thruster | 61 |
| 6.3.2 | FIB | 64 |
| 7 | Conclusions and Future Work | 65 |
| 7.1 | BMI-I ILIS | 65 |
| 7.2 | Ion Fragmentation | 66 |
| A | Drawings of the Full Beam Time of Flight Assembly | 67 |

List of Figures

| | | |
|------|--|----|
| 1-1 | The configuration of a basic capillary electrospray source. | 14 |
| 1-2 | The configuration of a basic ionic liquid ion source. | 15 |
| 2-1 | Diagram of a Taylor cone | 18 |
| 2-2 | Simplified FIB column | 23 |
| 3-1 | Scanning electron microscope image of an emitter tip | 26 |
| 3-2 | ILIS assembly with a copper block for temperature control | 26 |
| 3-3 | ILIS assembly using polyethylene blocks | 27 |
| 3-4 | Schematic view of the interleaved comb-type ion gate | 28 |
| 3-5 | Example TOF-MS Signal for an ILIS with two ion species | 29 |
| 3-6 | Schematic of the TOF-MS setup | 29 |
| 3-7 | Sample RPA output for a monoenergetic source | 31 |
| 3-8 | Sample RPA output for a nonideal source | 31 |
| 3-9 | Schematic of the RPA setup | 32 |
| 3-10 | Vacuum chamber | 33 |
| 4-1 | Current emitted from a BMI-I ILIS in the negative mode | 37 |
| 4-2 | TOF-MS signals for a BMI-I ILIS operating at several different conditions | 38 |
| 4-3 | Mass spectra for a BMI-I ILIS operating at (a) -1900 V and (b) 1900 V | 40 |
| 4-4 | RPA energy spectra results for applied voltages of -1.5, -1.6, and -1.7 kV | 41 |
| 4-5 | RPA energy spectrum results for applied voltages of -1.5 kV | 42 |
| 4-6 | Estimated angular intensity for a BMI-I ILIS | 43 |
| 5-1 | Cross section view of the vacuum chamber (dimensions in inches) | 46 |

| | | |
|------|---|----|
| 5-2 | Full beam TOF collector assembly | 47 |
| 5-3 | Schematic of the full beam TOF assembly | 48 |
| 5-4 | Non-inverting amplifier with a shunt resistor | 49 |
| 5-5 | Full beam TOF output with the original amplifier | 50 |
| 5-6 | Transimpedance amplifier | 51 |
| 5-7 | Optional caption for list of figures | 52 |
| 5-8 | Schematic of the full beam RPA assembly | 53 |
| 5-9 | Output of the full beam RPA with an EMI-BF ₄ ILIS operating at -1650V | 54 |
| 5-10 | Idealized energy distribution for an EMI-BF ₄ ILIS | 55 |
| 5-11 | Effect of beam divergence on an RPA current signal for an EMI-BF ₄ ILIS | 55 |
| 6-1 | RPA energy spectrum and current signal for a BMI-I ILIS operating at -1.5kV | 58 |
| 6-2 | Mean free path of non-solvated ions in an EMI-BF ₄ ILIS at 1500V . . | 60 |
| 6-3 | Effect of ion fragmentation on the polydispersive efficiency for an EMI- BF ₄ ILIS operating in the positive mode | 63 |
| A-1 | Full beam TOF front plate | 67 |
| A-2 | Full beam TOF secondary electron grid | 68 |
| A-3 | Full beam TOF collector | 68 |
| A-4 | Full beam TOF back plate | 69 |

List of Tables

| | | |
|-----|---|----|
| 1.1 | Properties of Selected Electrospray Source Media | 15 |
| 3.1 | Electronic equipment | 34 |
| 4.1 | Expected flight times for a BMI-I ILIS operating at +/- 2kV | 39 |
| 4.2 | Stopping potentials for products of ion fragmentation | 41 |

Chapter 1

Introduction

1.1 Electrospray Basics

Electrospray has been studied as a source of charged particles for applications ranging from materials analysis to space propulsion. The basic electrospray configuration is composed of a capillary tube filled with a conducting fluid facing an electrode plate, as shown in Fig. 1-1. Briefly, the source is operated by applying a voltage difference between the extractor plate and the capillary. The strong electric field at the liquid-insulator (commonly air or vacuum) interface causes the meniscus to deform into a conical shape, referred to as a Taylor cone after G.I. Taylor [21]. At the tip of the cone, the electric field is intense enough to cause the emission of ions or charged droplets, which are then free to accelerate to the extractor electrode. A more detailed description of the physics of an electrospray source is contained in Chapter 2.

The conducting fluid used in the electrospray source can be of several different varieties. Some commonly used liquids are doped solvents, liquid metals, and ionic liquids. In addition to the previously mentioned capillary tube emitters, externally wetted emitters can be used. In this configuration the liquid coats an electrochemically sharpened metallic (usually tungsten) needle. Capillary and electric forces cause the liquid to flow to the sharp tip, where the Taylor cone formation can occur. This thesis is concerned with the use of ionic liquids as the source media for an electrospray using an externally wetted emitter.

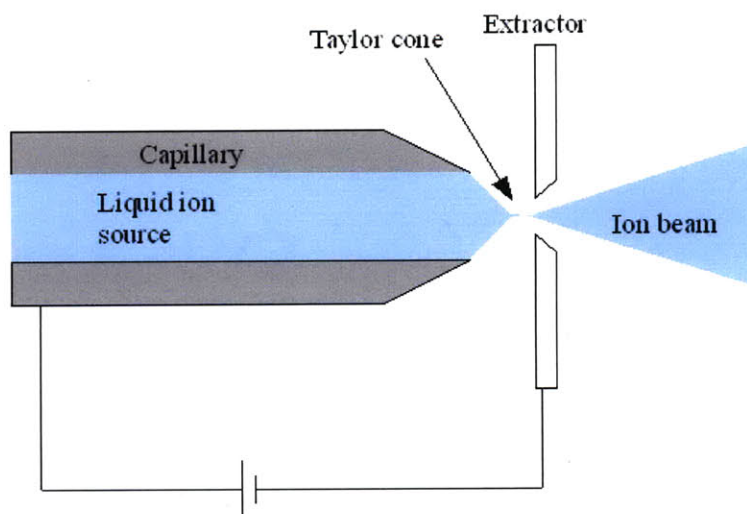


Figure 1-1: The configuration of a basic capillary electrospray source.

1.2 Ionic Liquids

Ionic liquids (ILs) are a type of salt that are in the liquid state at room temperature (sometimes specifically referred to as room temperature ionic liquids)[19]. Being a salt, these ILs are composed purely of positive and negative ions, with no solvent. Many ionic liquids have properties that make them an attractive choice for the use in an electrospray. Specifically, it is common for these ILs to have conductivities on the order of 1 S/m at room temperature and have negligible vapor pressures, which makes them ideal candidates for an externally wetted electrospray source operating in vacuum. The two ILs addressed in this thesis are 1-ethyl-3-methylimidazolium tetrafluoroborate ($[\text{C}_2\text{-mim}][\text{BF}_4]$ or EMI- BF_4) and 1-butyl-3-methylimidazolium iodide ($[\text{C}_4\text{-mim}][\text{I}]$ or BMI-I). Properties of these two ionic liquids are listed in Table 1.1 along with several other liquid ion sources. Notice the very large viscosity and low conductivity of BMI-I as compared to the other liquids. The ability to obtain significant currents from this liquid is something that does not mesh with current theories regarding the behavior of electrically stressed ionic liquids [10].

| Liquid | Melting Point (°C) | Surface tension (N/m) | Conductivity (S/m) | Viscosity (cP) |
|----------------------|--------------------|-----------------------|--------------------|----------------|
| Ionic liquids | | | | |
| EMI-BF ₄ | 12 | 0.052 | 1.3 (25°C) | 27.5(25°C) |
| | | | 2.3(50°C) | 12.6 (50°C) |
| BMI-I | <25 | 0.0547 | 0.069 (25°C) | 1100 (25°C) |
| | | | 0.25(50°C) | 500 (50°C) |
| Metals | | | | |
| Ga | 30 | 0.711 | >> 1 | 1.9 |
| In | 328 | 0.556 | | 2.55 |
| Cs | 29 | 0.071 | | 0.7 |

Table 1.1: Properties of Selected Electrospray Source Media

1.3 The Prototypical Ionic Liquid Ion Source

When an ionic liquid is used as the source media for an electrospray device and operated in a purely ionic mode, it can be referred to as an Ionic Liquid Ion Source (ILIS). The basic ILIS consists of an externally wetted needle emitter (normally fabricated from tungsten) coated with the ionic liquid. A high voltage is applied between the needle and a planar electrode with an aperture in it, referred to as the extractor. This causes charged particles to emit from the tip, and pass through the extractor. A diagram of this setup is shown in Fig. 1-2. The extracted ion beam is then able to be used for whatever application is required. It may be used in some sort of diagnostic equipment for characterization (Ch. 3 and Ch. 5), some propulsive application (Sec. 2.2.1), a focused ion beam application (Sec 2.2.2), or some other application.

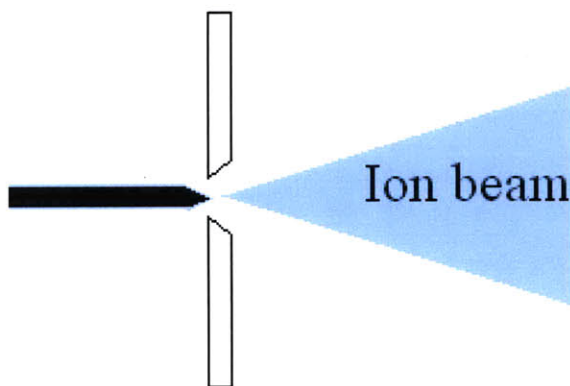


Figure 1-2: The configuration of a basic ionic liquid ion source.

Chapter 2

Electrospray Physics and Applications

2.1 Electrospray Physics

2.1.1 Taylor Cone Formation

When the meniscus of an electrically conductive liquid is subject to a strong electric field, the liquid surface becomes unstable and forms into a conical shape called a Taylor cone, as shown in Fig. 2-1. Details of the processes behind the formation of this feature can be found elsewhere [7, 21]. A simplified analysis of this structure can be performed if it is assumed to be static. In this case, the electrostatic traction must balance the surface tension at all points along the cone, given by

$$\frac{1}{2}\epsilon_0 E_n^2 = \frac{2\gamma}{R_c} \quad (2.1)$$

where E_n is the normal component of the electric field, γ is the surface tension of the liquid, and R_c is the radius of curvature of the liquid surface, which is related to the distance from the tip by $R_c = r \cot \alpha_T$. The conducting liquid surface is assumed static, and therefore an equipotential. The general solution to the Laplace equation in spherical coordinates for this geometry, assuming axial symmetry, is

$$\Phi(r, \theta) = \sum_{l=0}^{\infty} r^l P_l(\cos \theta) \quad (2.2)$$

where P_l is the Legendre function of order l . However, the restriction of Eq. 2.1 requires that the electric field at the cone surface to be proportional to $r^{-\frac{1}{2}}$, therefore the potential must be proportional to $r^{\frac{1}{2}}$. For the cone surface at $\theta = 180^\circ - \alpha_T$ to be an equipotential, $P_{\frac{1}{2}}(\cos(180^\circ - \alpha_T))$ must be zero. This requires $180^\circ - \alpha_T = 130.7^\circ$, resulting in the half angle of the Taylor cone being $\alpha_T = 49.3^\circ$.

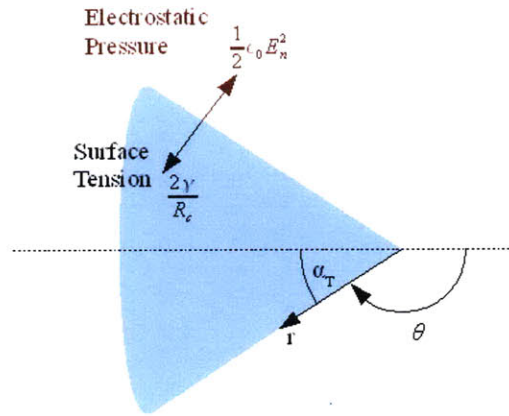


Figure 2-1: Diagram of a Taylor cone

However, in this model of a perfectly conical surface, the electric field will approach infinity as r goes to zero due to the $r^{-\frac{1}{2}}$ dependence. This is obviously a nonphysical solution, and something must break down. There are several possibilities for what occurs near the tip, two of which are the cone-jet mode, discussed in Sec. 2.1.2, and ion evaporation, discussed in Sec. 2.1.3.

2.1.2 Current Emission in the Cone-Jet Regime

In the region near the tip, the electric field becomes strong enough to overcome the liquid surface tension, and the static approximation breaks down. The details of what happens near the tip depend upon the exact operating parameters, but one possibility is called the cone-jet mode, which is characterized by the formation of a jet extending from the tip of the cone. This jet breaks up into droplets, which then

form the spray of charged particles. This cone-jet is perhaps the most studied of electro spray modes, with a large amount of literature focused on the regime [7, 2, 6]. The current produced in this regime has been found to depend on the flow rate Q , as well as the liquid's surface tension γ , conductivity K , and permittivity ε ,

$$I = f(\varepsilon) \left(\frac{\gamma K Q}{\varepsilon} \right)^{1/2} \quad (2.3)$$

The size of the jet at the tip of the Taylor cone has been seen to decrease in size as the conductivity of the liquid increases. When the conductivity of the liquid is high enough, it is possible for the cone to operate in a purely ionic regime, as seen with liquid metals [17] and certain ionic liquids [7, 14].

2.1.3 Field Evaporation of Ions

In an electro spray source with a high conductivity liquid source, such as a liquid metal or certain ionic liquids, it is possible for the tip of the Taylor cone to develop electric fields strong enough to cause the direct evaporation of ions. The current emitted in this manner can be characterized by Schottky's field-enhanced thermionic emission relation,

$$j = \varepsilon_0 E_n \frac{kT}{h} e^{-\frac{1}{kT} \left(G - \sqrt{\frac{q^3 E_n}{4\pi \varepsilon_0}} \right)} \quad (2.4)$$

where j is the current density, ε_0 is the permittivity of free space, k is the Boltzmann constant, T is the liquid temperature, h is Planck's constant, q is the ion charge, G is the solvation energy of the bound ion, and E_n is the electric field normal to the liquid surface. Copious ion emission will occur when the electric field satisfies the condition

$$E_n > \frac{4\pi \varepsilon_0 G_0^2}{q^3} \quad (2.5)$$

Typical values of G fall in the range of 1-3 eV [15], meaning that for extraction of singly charged ions, the electric field needs to approach 1 V/nm.

2.2 Electrospray Applications

2.2.1 Space Propulsion

Electrosprays have found applications in space propulsion in several different forms. Field Emission Electric Propulsion (FEEP) thrusters use an ion beam produced from an electro spray from a liquid metal (the previously mentioned LMIS). Colloid thrusters use a capillary source to spray droplets of ionic liquids or doped solvents [8]. Finally, ILIS based thrusters are being actively developed. ILIS sources can generally provide on the order of up to $1 \mu\text{A}$ and $0.1 \mu\text{N}$ per emitter. Therefore, current research into ILIS thrusters has been focusing on microfabrication of very dense arrays of emitters, in order to achieve higher thrust densities [4, 3, 12]. With these types of arrays, it is possible to approach thrust densities on a level with conventional ion engines [12].

An ILIS based thruster offers several attractive advantages as a means of space propulsion. The ionic liquid is composed of both positive and negative ions, which allows for the extraction of either type. This means that it is possible to simultaneously operate one ILIS in the positive mode and another in the negative mode in order to maintain electrical neutrality, eliminating the need for an external cathode neutralizer. They have been demonstrated to be operated with a variable specific impulse [4, 20], which would allow for flexible mission design. The propellant feed system for these thruster can be greatly simplified by using a porous substrate to fabricate the tips, and relying on capillary flow to move the liquid to the emitters [3]. Finally, the ILIS thrusters are able to operate at high thrust efficiencies, estimated to be up to 85%.

The details of the efficiency have been examined elsewhere [13], but are briefly mentioned here. The definition of thrust efficiency, η_T , is the thrust power divided by the supplied electric power

$$\eta_T = \frac{P_T}{P_E} = \frac{\frac{1}{2}F^2/\dot{m}}{IV_0} \quad (2.6)$$

where F is the thrust, \dot{m} is the mass flow rate, I is the power supply current and V_0 is the power supply voltage. The expression for the efficiency in Eq. 2.6 can be modified by defining several other terms. The ionization efficiency, η_i , is defined to be the mass fraction of ions emitted over the total mass flow rate (ions and neutrals). Ionic liquids have extremely low vapor pressure, so the neutral flux is almost zero, meaning $\eta_i \approx 1$. The transmission efficiency, η_{tr} , is defined as the mass ratio of ions leaving the device and producing thrust to the ions being emitted from the liquid. This term is less than one if any of the ions hit the extraction electrode on the way out. By properly aligning the emitter and extractor electrodes, the intercepted current can be reduced to below 1%, giving transmission efficiencies of $\eta_{tr} \geq 99\%$. The ions emitted from an ILIS will have some angular distribution, $f(\theta)$, about the axis. Previous studies have shown that the distributions can be approximated by a quadratic function given by Eq. 2.7 [13, 14].

$$f(\theta) = \frac{3}{2\theta_0} \left[1 - (\theta/\theta_0)^2 \right] \quad (2.7)$$

Only the portion of momentum from these particles that is directed along the axis will contribute to thrust, which is expressed through the angular efficiency. The angular efficiency η_θ is

$$\eta_\theta = \left[\int_0^{\theta_0} f(\theta) \cos(\theta) d\theta \right]^2 \quad (2.8)$$

where θ_0 is the beam envelope. For a typical ILIS divergence angle of about 20° , Eq. 2.8 gives $\eta_\theta \approx 0.98$, and for a less ideal case of 42° divergence the efficiency is still relatively high at $\eta_\theta \approx 0.90$. The energy efficiency, η_E , takes into account the conversion of electrical power into kinetic energy of the particles, and for ILIS thrusters it is generally very high, approximately $\eta_E \geq 0.98$ [13]. The final contribution to the efficiency is the polydispersive efficiency, η_p , which takes into account the energy wasted accelerating charged particles of different specific charges. An ILIS operating in the purely ionic regime will have ion species of the form $A^+(AB)_n$ or $B^-(AB)_n$ where n is the degree of solvation. For many ionic liquids, the $n = 0$ and $n = 1$ ions

will dominate the emitted beam. For this case of two ionic species, the polydispersive efficiency can be expressed as

$$\eta_p = \frac{[1 - (1 - \sqrt{\zeta}) f_0]^2}{1 - (1 - \zeta) f_0} \quad (2.9)$$

where ζ and f_0 are the specific charge ratio and the current fraction of non-solvated ions in the beam,

$$\zeta = \frac{(q/m)_1}{(q/m)_0} \text{ and } f_0 = \frac{I_0}{I_0 + I_1} \quad (2.10)$$

The polydispersive efficiency tends to be the most limiting factor in the efficiency of an ILIS thruster, but still be relatively high. For example, an EMI-BF₄ ILIS will typically produce an ion beam composed of approximately 50% pure ion and 50% singly solvated ($n = 1$) ion, with masses of 111.2 amu and 309.1 amu, respectively. With these values, Eq. 2.9 gives the polydispersive efficiency to be $\eta_p = 0.94$.

The total efficiency is expressed in terms of the individual efficiencies as

$$\eta_T = \eta_i \eta_{tr}^2 \eta_\theta \eta_E \eta_P \quad (2.11)$$

and for an ILIS can have values greater than 80%. This particular expression for the efficiency fails to take into account the effects of ion fragmentation, which is discussed in Ch. 6.

2.2.2 Focused Ion Beam Applications

Liquid metal ion sources, in particular the gallium LMIS, have been used extensively in the field of focused ion beams (FIB) [17]. FIB technology uses an ion beam focused to sub-micrometer dimensions to either examine or modify the surface of a target material. Applications include milling, material deposition, microscopy, and others [17, 9]. A basic FIB setup, as shown in Fig. 2-2 will have an ion source (typically a LMIS), some beam defining aperture, a lens to focus the beam, a method of deflecting the beam, and then the target. More practical systems often include multiple lenses,

filters, and more aberration corrections. As mentioned previously, the operations of an ILIS is very similar to that of an LMIS. For this reason, ionic liquid ion sources have been proposed to be used in FIB applications [24, 23, 18]. ILIS have several properties that make them very attractive for FIB applications, including low starting voltages, room temperature operation, and perhaps most importantly, the hundreds of available ionic liquids. Initial studies into using ILIS in FIB have been promising, and it is still an ongoing research subject.

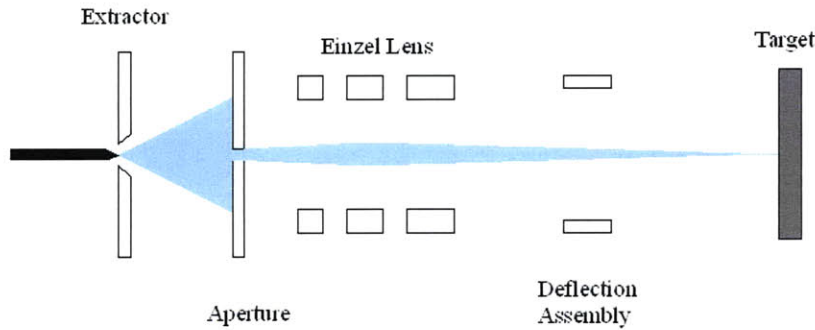


Figure 2-2: Simplified FIB column

One of the figures of merit of the performance of a focused ion beam system is the beam probe size (the size of the focused ion beam on the target). To be useful for FIB applications, the ion beam must be focusable down to micron or sub-micron levels [17]. There are many parameters that can affect the quality of the beam probe, but in general they can be split between properties of the ion source, and properties of the FIB system. The important parameters of the ion source are the angular intensity, the relative energy spread, and the source size. The angular intensity is defined to be the current per unit solid angle, $dI/d\Omega$, and can be related to the beam current by $I = \int \frac{dI}{d\Omega} d\Omega$. In a FIB column, the aperture angle α_0 is normally small, meaning the angular intensity can be approximated as a constant, and the current is obtained from

$$I = \Delta\Omega \frac{dI}{d\Omega} = 2\pi(1 - \cos \alpha_0) \frac{dI}{d\Omega} \approx \pi\alpha_0^2 \frac{dI}{d\Omega}. \quad (2.12)$$

The energy spread of the ion beam is characterized by the full width at half

maximum of its energy spectrum, $\Delta W_{1/2}$. The size of the source, D , may be on the order of nm, and the FIB optics may act to magnify or demagnify this.

The parameters of the FIB optics are the spherical aberration, C_s , the chromatic aberration, C_c , and the magnification, M . Each of these terms will contribute to the spot size of the focused ion beam. The contribution of the magnification is simply to magnify the source size, giving an effective spot size of

$$d_g = MD \quad (2.13)$$

The spherical aberration causes particles farther from the central axis to be focused more strongly than those that are closer. The effect of this term is that a point source will focus to a disc, rather than a point, with the size being given by

$$d_s = \frac{1}{2}\alpha_0^3 C_s \quad (2.14)$$

The chromatic aberration causes ions of differing energies to be focused onto different spots along the optical axis, with the minimum size of the focused spot being

$$d_c = \alpha_0 C_c \frac{\Delta W_{1/2}}{W}. \quad (2.15)$$

The combined effects of these effects on the focused spot size can be combined by summing in quadrature, to give

$$d^2 = d_g^2 + d_s^2 + d_c^2 \quad (2.16)$$

which can be expressed in terms of the beam current and brightness by using Eq. 2.12

$$d^2 = I^3 \frac{C_s^3}{\left[\pi M^2 \left(\frac{dI}{d\Omega}\right)\right]^3} + I \left(\frac{\Delta W_{1/2}}{W}\right)^2 \frac{C_c^2}{\pi M^2 \left(\frac{dI}{d\Omega}\right)} + M^2 D^2 \quad (2.17)$$

Chapter 3

Experimental Techniques

In order to characterize an ILIS device, several standard experimental techniques were employed. All of the described experimental setups described in this chapter were designed to be mounted on the Kimball Physics eV Parts system and then attached to a vacuum chamber flange, allowing for simple construction and alignment.

3.1 Ion Source

The ILIS used in all experiments described in this thesis is based on the externally wetted emitter design. The emitters were fabricated from a 0.5 mm DIA tungsten wire. The fabrication process is composed of several steps, based on the process described in Ref. [14]. The oxide layer on the wire is removed by an electrochemical etch in a 2 N NaOH solution using 5VAC for several seconds. The wire is then lowered into the solution by about 3 mm, and a 50 VDC etch is performed until the submerged portion of the wire is completely etched away. The needle tip is then shaped by etching under 15-25 VDC for 30-90 seconds. The surface of the emitter is then roughened by submerging it in a saturated solution of $K_3Fe(CN)_6$ in 1 N NaOH at 90°C. The resulting emitter has a roughened surface to promote wetting, and a tip radius on the order of 10 μm . An SEM image of an example tip can be seen in Fig. 3-1.

The emitter is then mounted in one of two custom-made systems. The first ar-

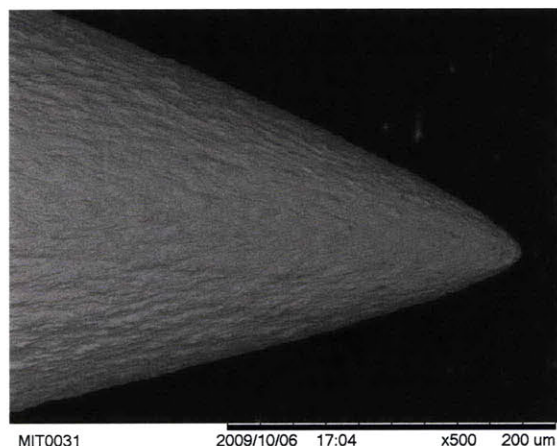


Figure 3-1: Scanning electron microscope image of an emitter tip

range ment consists of attaching the needle to a copper block. The copper serves as a point of electrical contact, as well as a heat sink. An electrical heater is attached to the block, with the temperature monitored by a K-type thermocouple. The block-emitter assembly is mounted on a 2-axis translational stage, which allows for alignment with the 1.5 mm diameter hole in the stainless steel extractor plate. A schematic of this setup is shown in Fig. 3-2. A tungsten crossbar is spot welded to the emitter a few mm from the tip, in order to allow a place for a liquid droplet reservoir to rest. Wetting is achieved by placing a drop of ionic liquid at the emitter tip, and allowing it to fall to the crossbar.

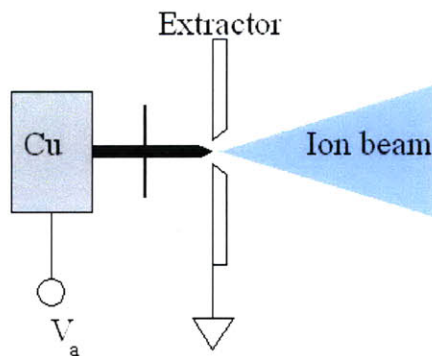


Figure 3-2: ILIS assembly with a copper block for temperature control

The second ILIS configuration consists of two polyethylene (PE) blocks. The first block has a small hole in the center, which allows an emitter to be held by a friction fit.

The second block has a stainless steel cylinder in the center, which holds a reservoir of ionic liquid. The extractor plate is placed after the second block. Alignment of all of the parts is ensured by mounting on alumina rods. Wetting of the emitter is performed by placing it into the first PE block, then sliding the emitter through the cylinder full of liquid in the second block.

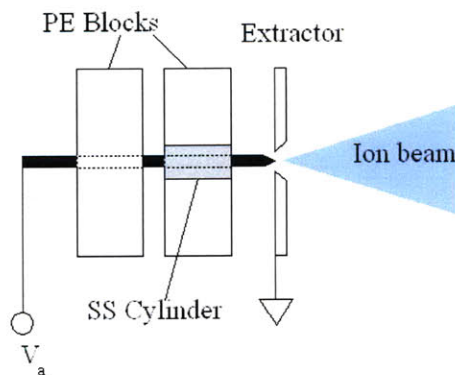


Figure 3-3: ILIS assembly using polyethylene blocks

The current passing through the emitter in either of these configurations is monitored by using a multimeter to monitor the voltage drop across a $100\text{k}\Omega$ resistor.

3.2 Time of Flight Mass Spectrometry

A charged particle of mass m and charge q accelerated through a potential, ϕ_a will have a kinetic energy given by

$$\frac{1}{2}mv^2 = q\phi_a. \quad (3.1)$$

Thus, for a beam of charged particles of unknown specific charge, accelerated through the known potential, the velocity will allow for the determination of the value of q/m . The velocity is determined by measuring the time, t , it takes for a particle to travel a known flight distance, L . The time is determined by gating the ion beam, and measuring the time it takes for the beam front to reach a collector plate. The gating is performed by an interleaved comb-type gate (also referred to as a Bradbury Nielsen

Gate or BNG). This type of gate consists of two sets of parallel wires which are set to ground potential when in the “off” mode, and equal in magnitude but opposite in sign potentials while in the “on” mode. The strong electric fields present between the wires when the gate is turned on cause the ion beam to deflect, but the fields decay quickly (within a few wire spacing distances) along the beam path. A schematic view of such a gate is shown in Fig. 3-4.

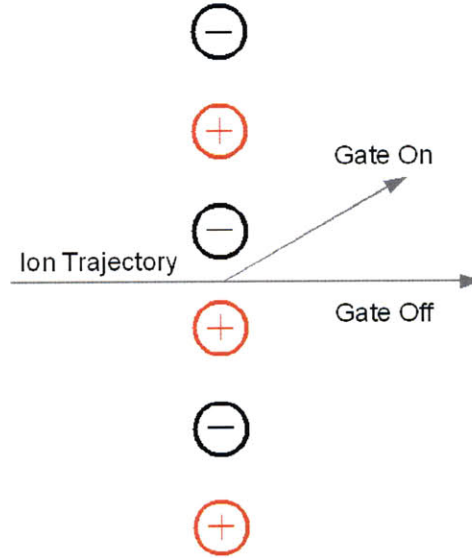


Figure 3-4: Schematic view of the interleaved comb-type ion gate

The gate is used to deflect the beam, and once the gate is switched off, allowing the beam to continue, the current at the collector plate is monitored. The time it takes the ions to reach the collector plate after the gate is switched off is given by

$$t = L \sqrt{\frac{1}{2} \frac{m}{q} \frac{1}{\phi_a}}. \quad (3.2)$$

However, as mentioned previously, the ion beam produced by an ILIS generally contains several species of ions with masses, $m_0, m_1, etc.$ and unit charge. Each of these ions will have a different flight time, given by Eq. 3.2. An example of the expected collector plate current signal is shown in Fig. 3-5. As seen in the figure, there are two distinct steps at times t_0 and t_1 corresponding to the masses of the ion species. The step size gives the relative amount of each ion in the beam. If there are

any droplets present in the beam, there will also be a continuous distribution of q/m values, showing up as a gradually sloped region in the TOF output.

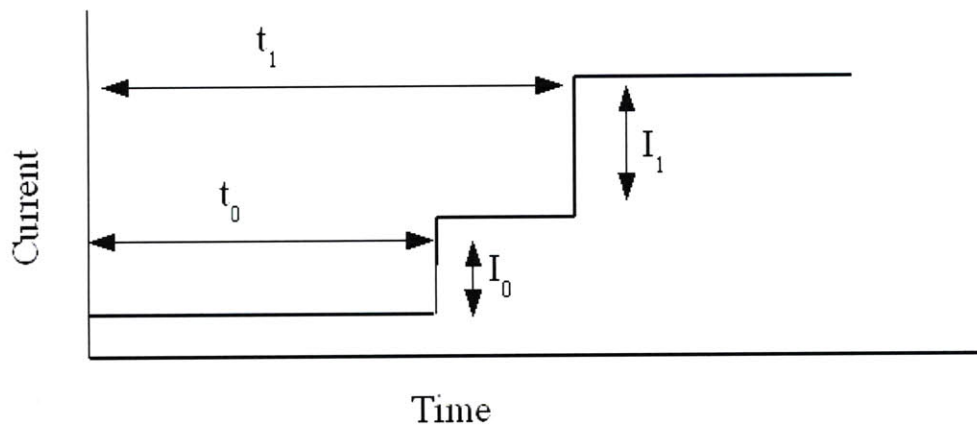


Figure 3-5: Example TOF-MS Signal for an ILIS with two ion species

The actual setup used for several experiments in this thesis is based on the design by Lozano [15, 16]. A schematic of the setup is shown in 3-6. In addition to the ion source and gate described previously, there is also an einzel lens. This lens serves to focus the ion beam, allowing for a longer flight distance, and therefore a higher resolution. Before the collector plate there are two grids. The first is grounded, while the second is biased to -30V in order to suppress secondary electrons at the collector.

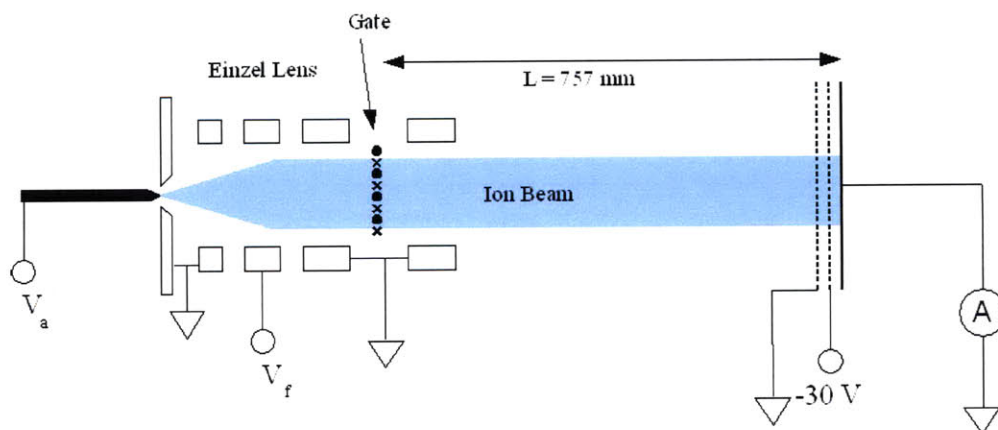


Figure 3-6: Schematic of the TOF-MS setup

3.3 Retarding Potential Analyzer

An ion that has mass m and charge q that has been accelerated from rest through a potential ϕ_a will have an energy $q\phi_a$. In order to prevent this particle from passing through a given region, an equal potential barrier of ϕ_a must be applied. In the case of an ILIS, the actual acceleration potential the ion sees is different than the applied extraction potential, ϕ_{ext} . It is of interest to find the actual energies of the ion beam in order to determine performance parameters of the ILIS, such as thrust efficiency in propulsive applications or the effects of chromatic aberration in focused ion beam applications, both of which were discussed in Sec. 2.2. In order to measure the energy, the ion beam is passed through a region with a controllable retarding potential, with a collector plate beyond the potential barrier. Such a device is referred to as a retarding potential analyzer (RPA). As the RPA voltage, ϕ_{RPA} , is varied, only those particles that satisfy the following equation will be collected, assuming ϕ_a , q , and ϕ_{RPA} all have the same sign.

$$|\phi_a| = \left| \frac{\frac{1}{2}mv^2}{q} \right| \geq |\phi_{RPA}| \quad (3.3)$$

So, for a completely monoenergetic ILIS ion beam, the current collected by the RPA as the voltage is swept from zero to ϕ_{ext} will be that shown in Fig. 3-7. As seen in the figure, the current is constant until the retarding potential reaches the beam potential, at which point all of the current is prevented from reaching the collector plate. The energy deficit D , assuming unit charge as with most ILIS, is given by the difference between the extraction potential and the stopping potential,

$$D = q(\phi_{ext} - \phi_a) \quad (3.4)$$

For a nonideal ILIS, the RPA signal will not actually look like that as shown in Fig. 3-7, instead it will look more similar to that shown in Fig. 3-8. The step corresponding to the acceleration potential will have finite width about the ideal location. There will also be secondary features in the signal, such as a secondary step

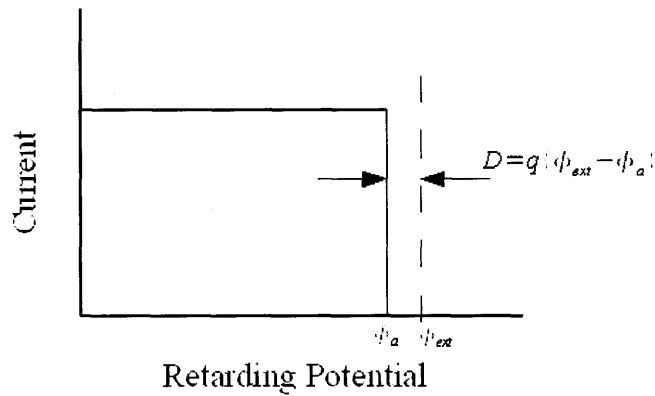


Figure 3-7: Sample RPA output for a monoenergetic source

at a lower voltage. This step is due to the fragmentation of solvated ions after being extracted. For example a singly solvated ion of mass m_1 may break up into an ion of mass m_0 and a neutral. Only the ion will be detected by the RPA, and it will be traveling at the same speed as before the breakup, meaning that it will be stopped by a potential given by

$$\phi_s = \frac{m_0}{m_1} \phi_a. \quad (3.5)$$

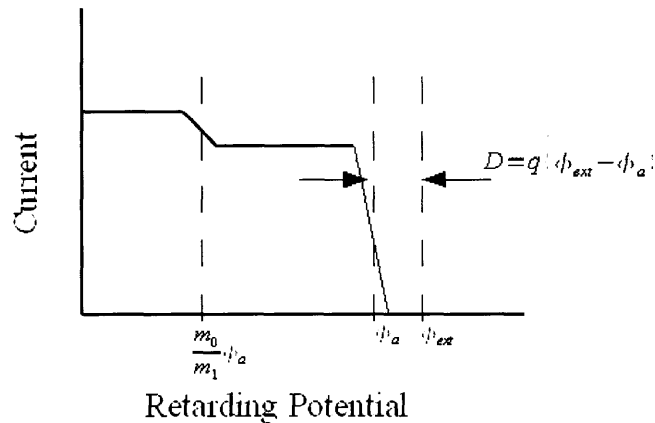


Figure 3-8: Sample RPA output for a nonideal source

In order to obtain the energy distribution from an RPA signal, the derivative of the curve as shown in Fig. 3-7 can be taken.

The experimental setup used for the RPA is based on the design in Ref. [16]. As with the TOF-MS, an einzel lens is positioned 8.8 mm from the extractor. The lens serves to collimate the beam, in order to eliminate energy spread due to beam divergence. After the lens is a grounded aperture and a shielded drift region of 12 mm. The RPA itself is at the end of the drift region. The basic form of the instrument is taken from Ref. [25], and consists of a 25 mm inner diameter and 25 mm length stainless steel cylinder placed within a grounded enclosure. Immediately prior to the cylinder is a grounded plate with an entrance aperture of 3 mm diameter. At the other end of the cylinder are a series of grids composed of $76 \mu\text{m}$ diameter tungsten wire with spacing of 0.76 mm, giving a transparency of 90 % for each grid. The collector used in the RPA is a Faraday cup connected to an oscilloscope through a high impedance electrometer. The RPA is operated by applying a low frequency (33 mHz) high voltage triangular wave to the grids and cylinder. Postprocessing of the collected signal involves low-pass filtering to eliminate noise, followed by a second-order finite difference scheme to obtain the energy distribution.

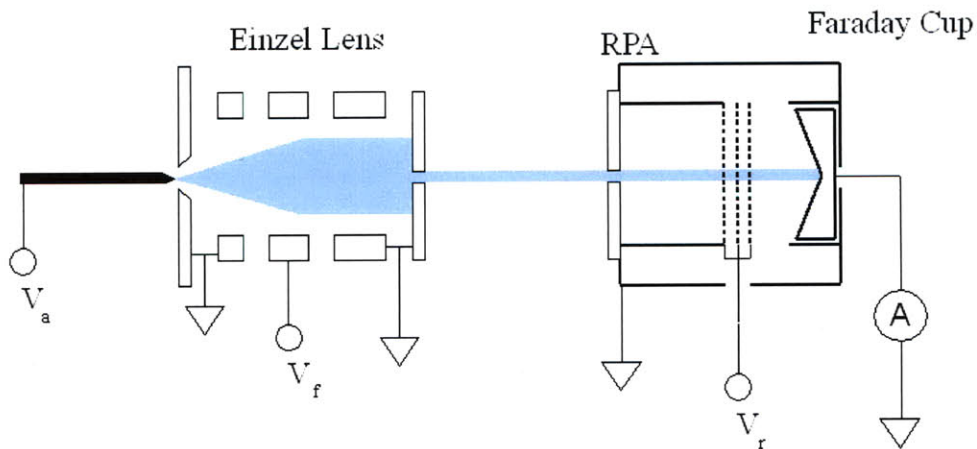


Figure 3-9: Schematic of the RPA setup

3.4 Vacuum Chamber and Electronics

All experiments took place in a vacuum chamber at pressures below 5×10^{-6} . The chamber itself, shown in Fig. 3-10, is a cylinder constructed of stainless steel. The main portion of the chamber has a 19.7 cm inner diameter and a length of 49.5 cm. Attached to the back of the chamber is an extension tube of inner diameter 5.6 cm and length of 36.5 cm. The chamber is evacuated using two Varian V-70 turbopumps, with a Varian SD-40 mechanical pump providing the necessary back pressure. Pressure inside the chamber is measured using either a Varian IMG-100 cold cathode gauge or a Varian 571 Bayard-Alpert type ionization gauge.

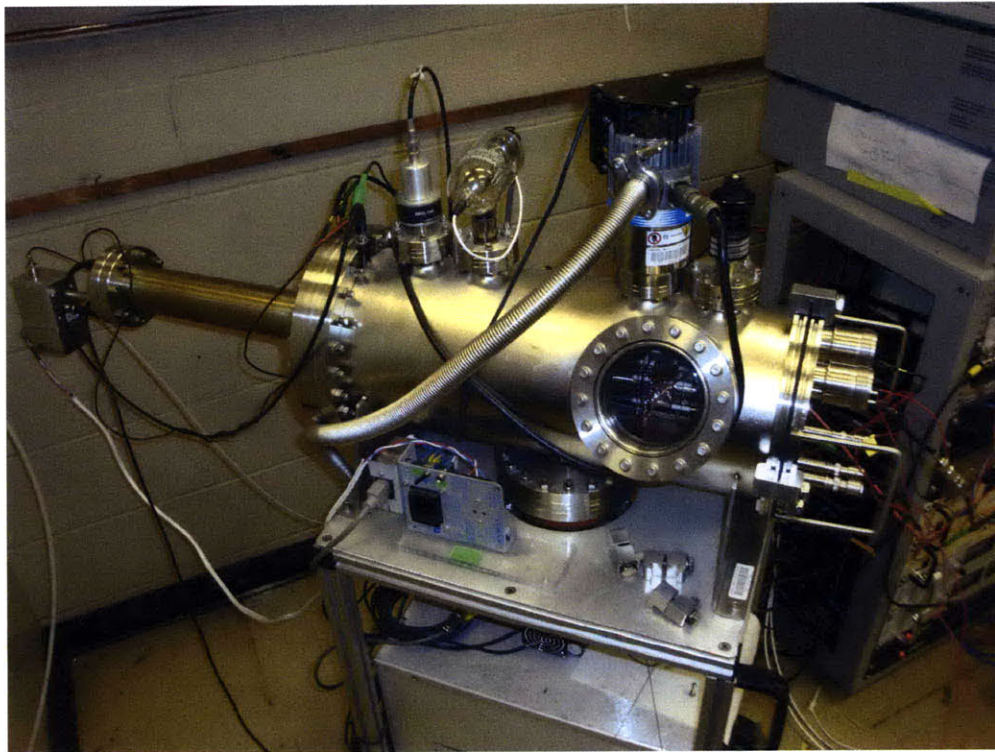


Figure 3-10: Vacuum chamber

The electronics used in all the experiments are listed in Table 3.1

Table 3.1: Electronic equipment

| | |
|-----------------------------|---|
| High Voltage Power Supplies | 2 x Matsusada AMS-5B6 Bertan 205B-05R Bertan 205B-10R |
| Lab Power Supply | Tenma 72-6615 |
| Oscilloscope | Agilent Infiniium 54835A |
| Electrometers | Keithley 6517 Keithley 6514 |
| Pulse Generator | BNC-555 |
| Pulse Amplifier | DEI PVM-4210 |

Chapter 4

Development of an Iodine ILIS

4.1 Motivation

As mentioned previously, the use of ILIS in FIB is very appealing partially due to the incredible variety of ionic liquids that are available. The choice for the study of this particular ILIS, using the ionic liquid 1-butyl-3-methylimidazolium iodide is motivated by the possibility of creating a beam of iodine ions. Though there may be many uses for such an ion beam, there are two particular applications that are in mind when investigating this ILIS.

The first is the use of an iodine beam to etch type III-V semiconductors, a class of material including GaAs, InP, InSb and several others. The reactivity of iodine with several of the component elements in the III-V group make it an attractive choice for etching. The concept of using iodine for this purpose is nothing new, as it is commonly used assist to FIB etching by injection of iodine gas in a process called gas assisted etching (GAE) [11]. There have also been studies of directly using a positive iodine ion beam for etching III-V materials [5], which showed it to be effective when milling indium-containing semiconductors. This history of using iodine for milling and GAE of these semiconductor materials is a strong motivation for this study.

The second application in mind is for the use in secondary ion mass spectrometry (SIMS). In SIMS, the surface of some sample is bombarded with ions, resulting in the creation of secondary ions which can then be analyzed using mass spectrometry

techniques. There are several ion sources that can be used in SIMS, but only a few different sources are available using negative ions. An iodine source is attractive for this application because the relatively massive iodine particles would have a good yield of secondary ions. A negative iodine source using surface ionization of iodine gas has been previously constructed for this application [22], however the simplicity of an ILIS makes it an attractive option.

4.2 Beam Characterization

With the guidelines from Sec. 2.2.2 in mind, the ion beam produced by a BMI-I ILIS is investigated to determine the properties relevant to operation in a FIB system. The experimental techniques discussed in Chapter 3 are used for this characterization, with the ion source configuration being that shown in Fig. 3-2. Two different emitters were used during the testing of the BMI-I ILIS, hereafter referred to as emitter A and emitter B. The majority of experiments were performed with the ILIS operating in the negative mode, due to the desire to create a beam of iodine ions as discussed in Sec. 4.1, however some data on the positive mode is included for completeness.

Previous studies with this particular ionic liquid [23] were unable to achieve stable current emission at room temperatures. In order to perform the experiments described in this chapter, the ILIS had to be heated to 50°C to achieve stable emission. Unless otherwise mentioned, all data presented was collected at this operating temperature. After successfully achieving stable current, initial tests were performed to simply measure the emitted current versus the applied extraction voltage. An example I-V curve obtained is shown in Fig. 4-1. Emission began at voltages lower than shown, but was stable only in the range of about -1.5 to 1.9 kV for this particular emitter (emitter B). Other emitters have been operated at both lower and higher voltages, therefore the curve shown in the figure should be taken only as an example.

Perhaps the most significant implication from this measured current is that it was obtained at all. As seen in Table 1.1, the viscosity of BMI-I is about 20 times larger than EMI-BF₄ and its conductivity is about 5 times smaller. Despite these significant

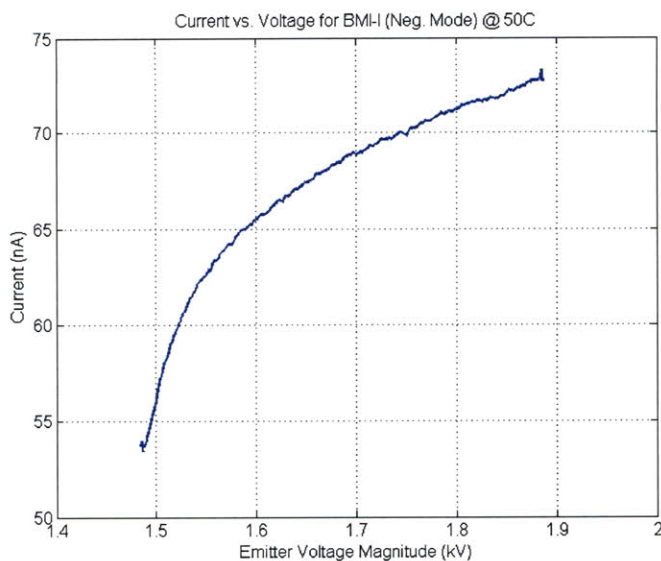


Figure 4-1: Current emitted from a BMI-I ILIS in the negative mode

difference, the current obtained from this BMI-I ILIS was only about 4 times lower than those seen with the well studied EMI-BF₄. This result is something that should be investigated further in the future.

4.2.1 Beam Composition

The composition of the ion beam was determined by using the time of flight mass spectrometry technique described in Sec. 3.2. Two sets of experiment studying the beam composition were performed. The first, with emitter A, varied the operating temperature and observed the mass spectra. The second, performed with emitter B, varied the operating voltage. Several plots of the current signal collected from the TOF-MS instrument for the BMI-I ILIS operating at +/- 2kV are shown in Fig. 4-2. A summary of the species observed can be seen in Table 4.1. As seen with prior studies of ILIS, the charged species contained in the beam are found to be singly charged ions attached to a number of neutrals, being of the form (BMI-I)_nBMI⁺ in the positive mode and (BMI-I)_nI⁻ in the negative mode. There is a strong presence of degree of solvation $n = 0, 1$ species, and signs of a small amount of $n = 2$ in some of these signals. Of particular interest in the figures are the plots for the ILIS in the

negative mode, where nearly half of the current signal is composed of I^- ions, without any sign of droplets.

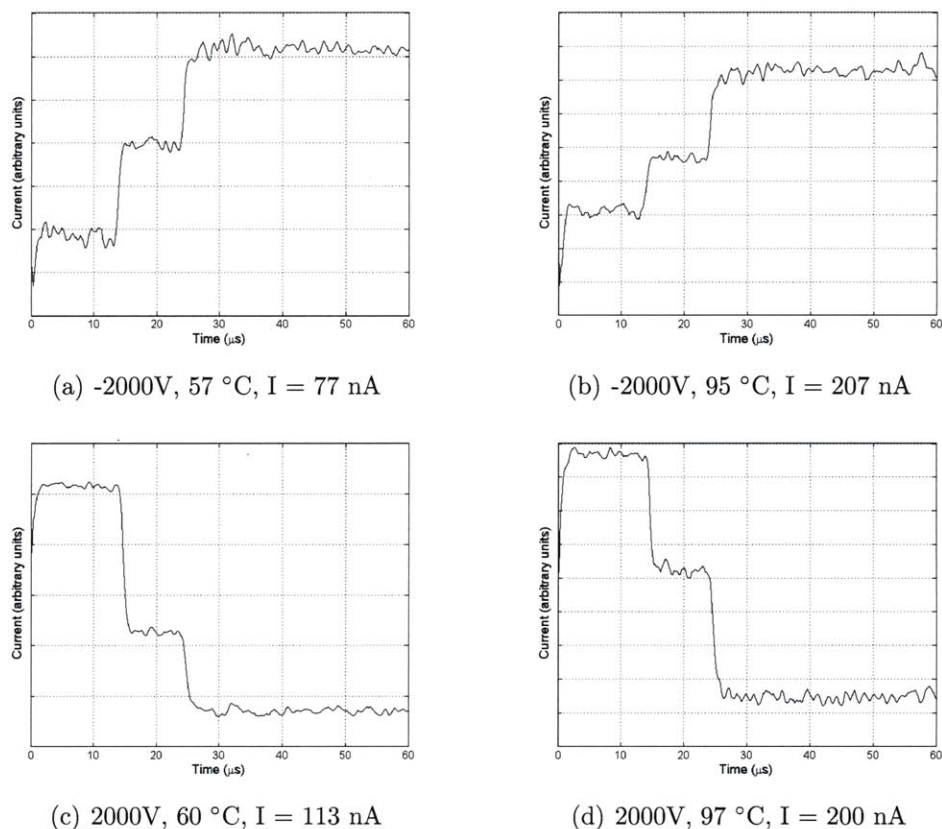


Figure 4-2: TOF-MS signals for a BMI-I ILIS operating at several different conditions

A second set up TOF-MS tests were performed for a second emitter (emitter B) operating in the range of 1.5 to 1.9 kV in both the positive and negative modes. The output data was subjected to a postprocessing scheme to convert the horizontal axis from time to mass using Eq. 3.2, followed by low-pass filtering and a finite difference differentiation to obtain the mass spectrum of the ILIS, showing “peaks” rather than a current signal. Results of this are shown in Fig. 4.2.1. There are distinct peaks corresponding to the non-solvated and singly solvated ions in both the positive and negative modes. Again, nearly half of the signal is composed of pure iodine ions in the negative mode.

| Polarity | Ionic Species | Ion Mass (amu) | Time of flight (μs) |
|----------|---------------------------------------|----------------|----------------------------------|
| + | BMI ⁺ | 139 | t0 |
| | (BMI-I)BMI ⁺ | 404.9 | t1 |
| | (BMI-I) ₂ BMI ⁺ | 670.8 | t2 |
| - | I ⁻ | 126.9 | t0 |
| | (BMI-I)I ⁻ | 392.8 | t1 |
| | (BMI-I) ₂ I ⁻ | 658.7 | t2 |

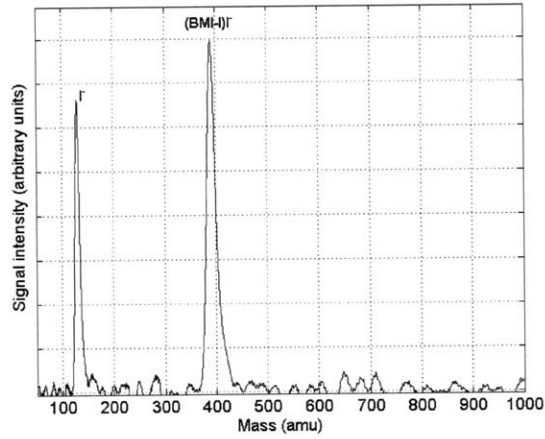
Table 4.1: Expected flight times for a BMI-I ILIS operating at +/- 2kV

4.2.2 Energy distribution

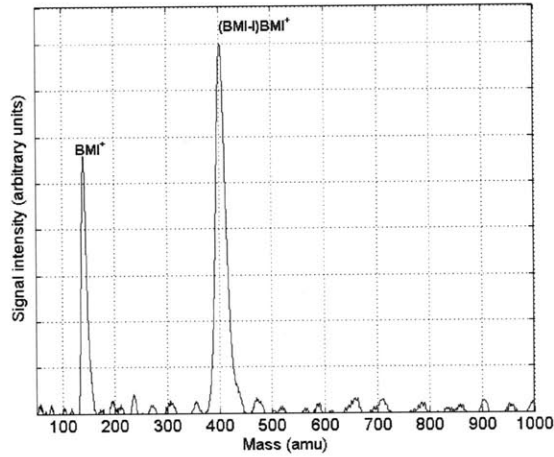
The energy distribution of the ion beam operating in the negative mode was determined by the use of the RPA as described in Sec. 3.3. Representative energy spectra for applied potentials of -1500, -1600, and -1700 V are shown in Fig. 4-4.

These show distinct peaks at potentials slightly below the applied extraction voltage. The energy deficit, D , ranges from 9 to 15 eV in these case. The full width at half max (FWHM) in these cases are about 12 eV. These values are significantly higher than those seen with previous studies on the energy distributions of ion beams from an ILIS. For example, a study with the ionic liquid EMI-Im found deficits of about 6 eV and FWHM of about 7 eV [16].

In addition to the primary signal in the energy spectrum, some secondary features are also present as seen in Fig. 4-5. There are two secondary peaks, located at potentials corresponding to the breakup of the $n = 2$ ion into $n = 1$ and of the $n = 1$ ion into $n = 0$. As described by Eq. 3.5, the locations of these peaks correspond to the mass ratios of the initial and final ions, whose values are listed in Table 4.2. Other than the primary peak and the two secondary peaks, there is also a slight, more or less constant signal contained between the $n = 1 \rightarrow 0$ and primary peaks. A continuous energy distribution can sometimes be due to droplets, but the TOF-MS showed only ions. Also, the containment of this continuous signal between the two peaks suggests that it is due to ion fragmentation in the region between the emitter and extractor. This fragmentation is discussed in more detail in Ch. 6.



(a)



(b)

Figure 4-3: Mass spectra for a BMI-I ILIS operating at (a) -1900 V and (b) 1900 V

4.3 Estimated Performance in a FIB Column

With the BMI-I ILIS well characterized for operation in the negative polarity, it is possible to use Eq. 2.17 to make an estimate of the performance in a FIB column. The values that are required from the ILIS are the current, the angular intensity $\frac{dI}{d\Omega}$, the beam energy spread, $\Delta W_{1/2}$, and the beam energy, W . The aberration coefficients, C_s and C_c , and the magnification, M , are properties of the FIB column, and not dependent on the ion source used. If the angular distribution of the beam is assumed to be parabolic with a half-angle of 18° as with other ILIS [14], then the angular

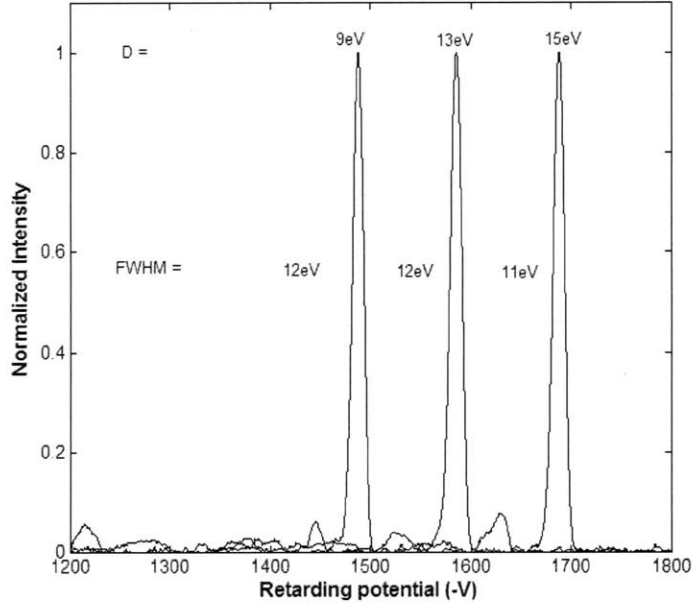


Figure 4-4: RPA energy spectra results for applied voltages of -1.5, -1.6, and -1.7 kV

| Initial → final degree of solvation | ϕ_{stop}/ϕ_a | ϕ_{stop} for $\phi_a = -1490$ V |
|-------------------------------------|----------------------|--------------------------------------|
| 1 → 0 | 0.32 | -477 |
| 2 → 1 | 0.60 | -894 |
| 2 → 0 | 0.19 | -283 |

Table 4.2: Stopping potentials for products of ion fragmentation

intensity for the BMI-I ILIS operating at a total current I_0 can be determined by relating the total current to the angular distribution, then taking the derivative with respect to the solid angle. First of all, the relationship between the half angle, α_0 , and the solid angle, Ω , for an axisymmetric layout is

$$\Omega = 2\pi(1 - \cos \alpha_0) \quad (4.1)$$

Therefore, the angular intensity can be written as

$$\frac{dI}{d\Omega} = \frac{dI}{d\alpha_0} \frac{d\alpha_0}{d\Omega} = \frac{1}{2\pi \sin \alpha_0} \frac{dI}{d\theta} \quad (4.2)$$

The current that is allowed to pass through an aperture of half angle α_0 can be

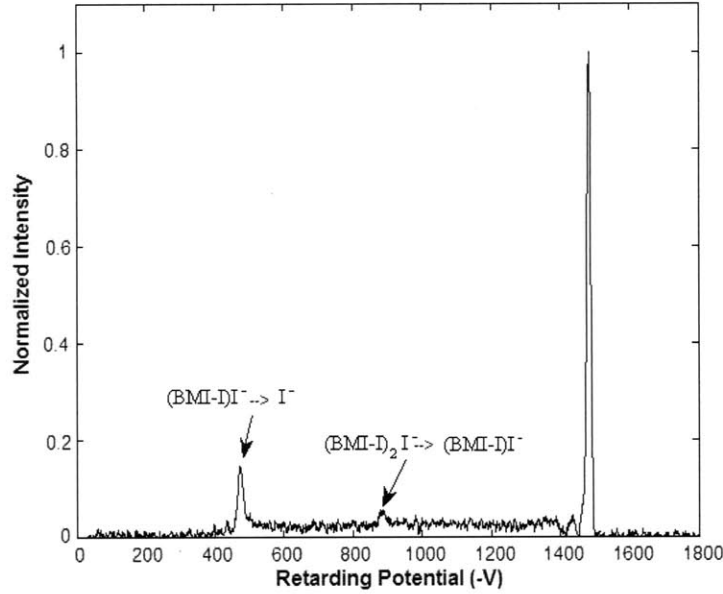


Figure 4-5: RPA energy spectrum results for applied voltages of -1.5 kV

determined by integrating the distribution function, $f(\theta)$, through the appropriate solid angle.

$$\frac{I_{\alpha_0}}{I_0} = \frac{\int_0^{\alpha_0} f(\theta) \sin(\theta) d\theta}{\int_0^{\theta_0} f(\theta) \sin(\theta) d\theta} \quad (4.3)$$

Thus the angular intensity at angle α_0 is found to be

$$\frac{dI}{d\Omega} = \frac{I_0}{2\pi} \frac{f(\alpha)}{\int_0^{\theta_0} f(\theta) \sin(\theta) d\theta} \quad (4.4)$$

A plot of the angular intensity versus the aperture angle is shown in Fig. 4-6. It can be seen that for the small angles typical of a FIB system (less than 10 mrad), the angular intensity is just below $0.65 \mu\text{A sr}^{-1}$.

Consider the performance of this BMI-I ILIS as compared with a LMIS operating in an optical column at unity magnification with spherical and chromatic aberrations of 1000 and 10 mm, respectively. The beam limiting aperture will be a small angle, so the relation between the current and angle can be simplified to

$$I = \Delta\Omega \frac{dI}{d\Omega} = 2\pi(1 - \cos \alpha_0) \frac{dI}{d\Omega} \approx \pi\alpha_0^2 \frac{dI}{d\Omega} \quad (4.5)$$

For the sake of comparison, assume the half angle of the aperture is sized to allow 100 pA of current through, corresponding to $\alpha_0 = 7$ mrad. Under these conditions and operating at a beam potential of 1500 V, the spot size would be approximately 300 nm, giving a current density of 0.15 A cm^{-2} . A typical Ga LMIS, for example, has brightness of $20 \mu\text{Asr}^{-1}$, an energy spread of about 5 eV, an operation energy on the order of 10^4 eV, and source size of around 50 nm [17]. This example LMIS would produce a spot of about 50 nm, with current density of 5 A cm^{-2} under the same conditions.

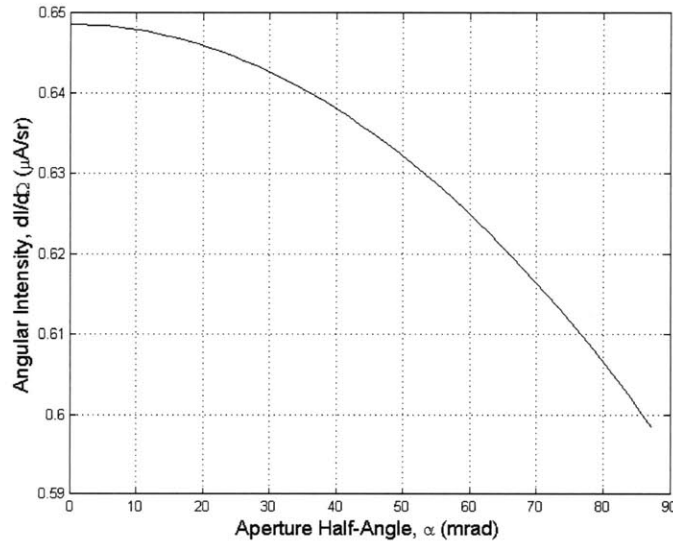


Figure 4-6: Estimated angular intensity for a BMI-I ILIS

Chapter 5

Full Beam Measurements

The experimental techniques described in Chapter 3 are designed to analyze only a portion of the ion beam from an ILIS. In order for this information to be used to characterize the ILIS itself, the ion beam needs to be assumed to be uniform, or the instrument needs to be scanned through the entire beam. It is desirable to have information on the entire beam, especially when looking at certain phenomena, such as the ion fragmentation briefly mentioned in Ch. 4. An alternative to these previously described techniques is to take measurements on the entire ion beam simultaneously, rather than just a portion. This chapter explores the design and testing of such an instrument, as well as the issues with taking such measurements.

5.1 Full Beam Time of Flight

The time of flight mass spectrometry setup described in Sec. 3.2 has a flight length of 757 mm. This long distance allows for a higher resolution TOF, but requires the use of an einzel lens to collimate the beam, in order to have a good signal at the collector plate. An issue with the use of an electrostatic lens is that it has a significant amount of chromatic aberration [17]. The effect is that only a certain range of energies are focused properly onto the collector plate. In the ideal situation, where there are only a few ionic species in a very narrow energy range, this does not cause any problems. However, for broad energy distributions, this may be an issue.

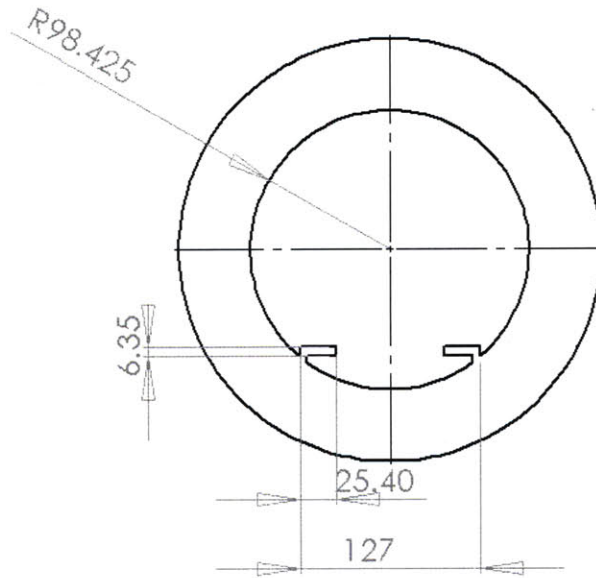


Figure 5-1: Cross section view of the vacuum chamber (dimensions in inches)

In order to address this issue, a full beam time of flight collector was designed. The design was limited by two main considerations. The first was that the instrument must fit into the current vacuum system, which is shown in cross-section view in Fig. 5-1. The second was that the half angle of collection should be about 20° to maximize the portion of the beam collected, which is based previous studies of ILISs [14]. Based on these two parameters, the design shown in Fig. 5-2 was created. More detailed drawings are contained in Appendix A.

This design has two grids of 70% transparency (8.66 holes per cm, wire thickness of 0.19 mm) followed by a collector plate. The first grid is grounded to serve as a shield, while the second grid is biased to -30 V to suppress secondary electrons. Following the two grids is a collector plate, which is connected to an amplifier. After the collector is a grounded back plate, which provides structural support as well as additional shielding. The distance between all plates is set to 6.35 mm using alumina spacers. With this setup, and a flight distance of 198.1 mm between the gate and collector as shown in Fig. 5-3, a half-angle of about 18° is collected. The collector assembly can be moved to decrease the flight distance (to have a larger collection

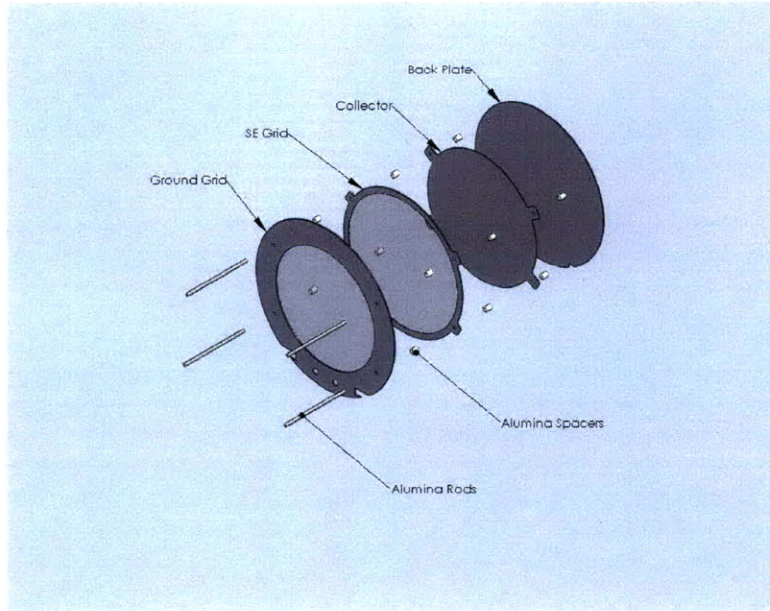


Figure 5-2: Full beam TOF collector assembly

angle) or to increase the distance (to have less beam spreading).

The collection half-angle of 18° will cause the TOF signal to have some spread due to the difference in time it takes ions at different angles to reach the collector. For a flight distance L and accelerating voltage V , an ion of mass m and charge q will have a flight time given by

$$t_0 = L \sqrt{\frac{1}{2} \frac{m}{q} \frac{1}{V}}. \quad (5.1)$$

if it has a trajectory that is parallel the axis of symmetry as shown in Fig. 5-3. However, if the ion's trajectory is inclined to an angle θ with respect to the axis, the flight time will be increased to

$$t_\theta = \frac{L}{\cos\theta} \sqrt{\frac{1}{2} \frac{m}{q} \frac{1}{V}}. \quad (5.2)$$

Therefore, the TOF signal will have a spread given by the difference between Eqs. 5.2 and 5.1. For example, an EMI-BF₄ ILIS operating in the positive mode at 1500 V will have an expected spread of about 0.2 μ s.

Initial tests of the full beam TOF were performed by connecting the collector

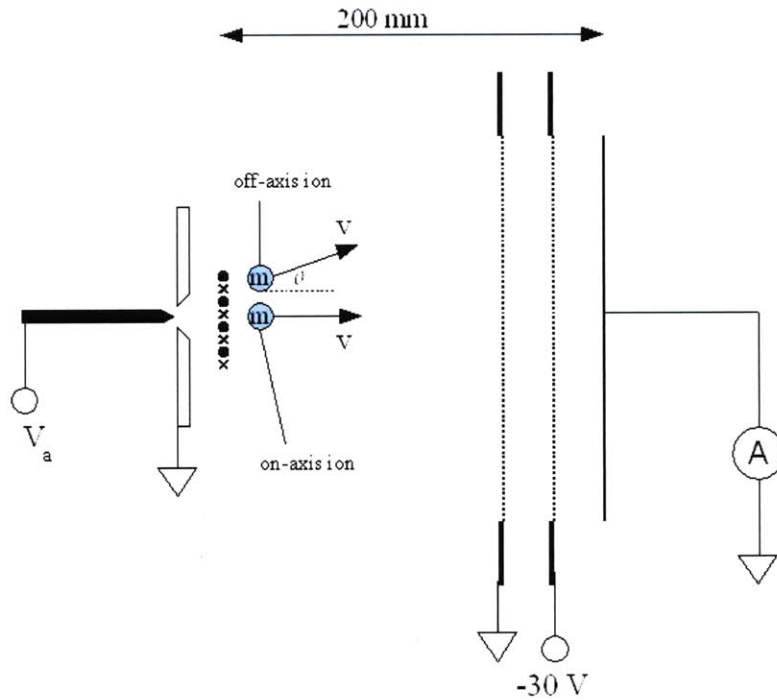


Figure 5-3: Schematic of the full beam TOF assembly

plate to ground through a shunt resistor, and amplifying the voltage drop across the resistor using a non-inverting amplifier with output to an oscilloscope, as shown in Fig. 5-4.

An example of the output from the amplifier, as recorded by an oscilloscope is shown in Fig. 5-5 for an EMI-BF₄ ILIS operating in the negative mode at -1500V, with a flight distance of approximately 266.7 mm. Under these conditions, the flight times of BF₄⁻ and (EMI-BF₄)BF₄⁻ are calculated to be 4.6 μ s and 8.4 μ s, respectively. As can be seen in the figure, there aren't any discrete steps as are expected for a TOF signal. However, at the expected locations of the steps are "shoulders" on the curve, followed by a region that appears to be an exponential decay. The fact that there are features that correspond to the expected step locations, and that there is an apparent exponential region suggests that the issues are due to increased capacitance in the circuit, when changing from the configuration described in Sec. 3.2.

In order to properly operate the full beam TOF, several different amplification

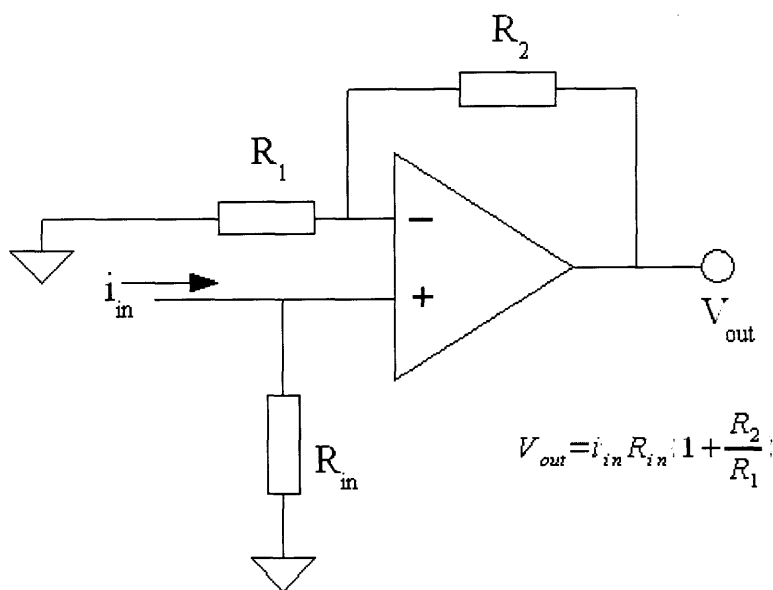


Figure 5-4: Non-inverting amplifier with a shunt resistor

circuits were considered, finally settling on a transimpedance amplifier as shown in Fig. 5-6. The op-amp chosen for the circuit was a Texas Instruments OPA637, paired with a $100\text{k}\Omega$ feedback resistor and a 2pF feedback capacitor. These components give the circuit a gain of 10^5 V/A, or in more relevant figures, $1\text{ mV} / 10\text{ nA}$. The bandwidth of the circuit will be given by the RC time constant, which in this case is $\tau = 0.2\mu\text{s}$ corresponding to about 0.8 MHz .

A EMI-BF_4 ILIS was used to test the setup, with representative signals shown in Fig. 5-7. The steps corresponding to BF_4^- and $(\text{EMI-BF}_4)\text{BF}_4^-$ are present in the negative mode, and those corresponding to EMI^+ and $(\text{EMI-BF}_4)\text{EMI}^+$ are present in the positive mode. The steps have a spread on the order of $0.2\ \mu\text{s}$, which could be due either to beam spreading or to the limited bandwidth of the amplifier. Also present in these plots, particularly in the negative mode, is a gradually sloped region after the initial steps, which may indicate the presence of droplets.

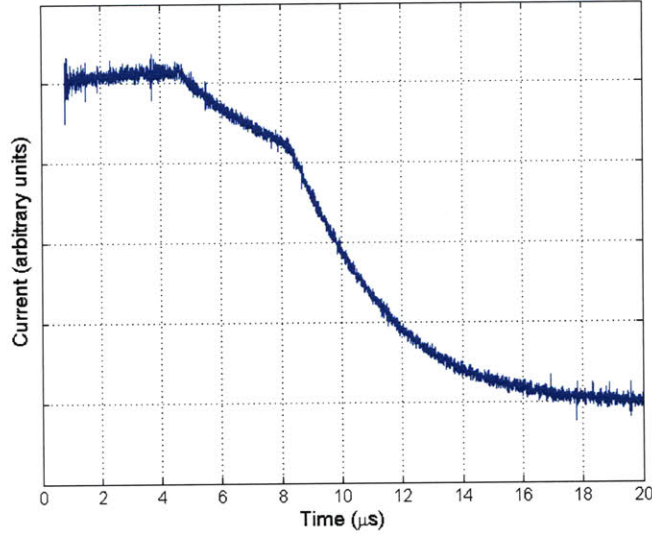


Figure 5-5: Full beam TOF output with the original amplifier

5.2 Full Beam Retarding Potential Analyzer

Although originally designed to be a TOF collector plate, the instrument described in Sec. 5.1 can also function as a coarse full beam retarding potential analyzer.

An ion with energy $\frac{1}{2}mv^2 = q\phi_a$ should ideally be stopped by a potential barrier ϕ_a . However, an ion with a trajectory at an angle θ relative to the axis will actually be turned around, but not brought to a stop, by a potential barrier of

$$\phi_{RPA} = \phi_a \cos^2 \theta. \quad (5.3)$$

This means that a full beam planar RPA will actually cause some artificial spreading in the measured energy spectrum.

An example output current signal of the full beam RPA from an EMI-BF₄ ILIS is shown in Fig. 5-9. The general shape of the curve is what is expected. There is a large drop in current near the extraction potential and a smaller drop due to the fragmentation of solvated ions. The nearly linear region between the two steps is attributed to fragmentation in the acceleration region, discussed in Ch. 6. However, unlike earlier studies, the width of the main step is seen to be very wide, greater than

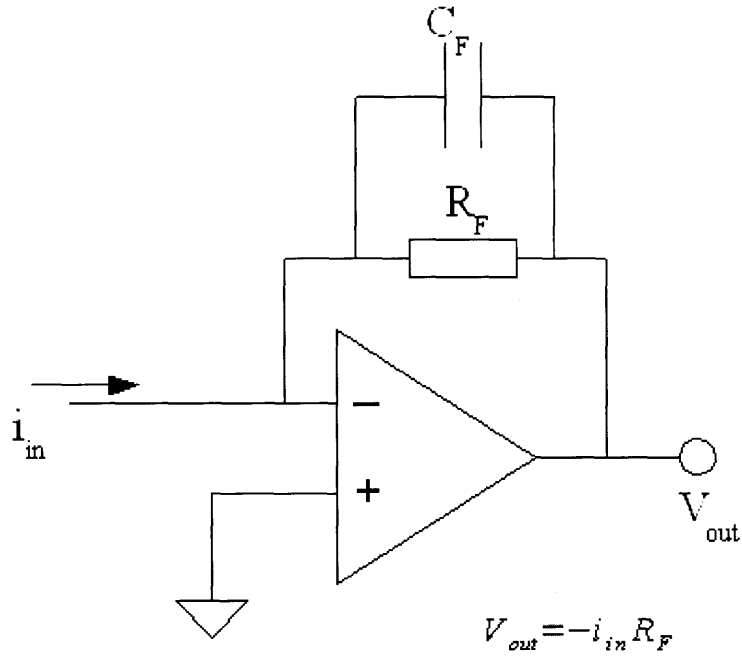


Figure 5-6: Transimpedance amplifier

100V. This spreading is due to the effect of a divergent beam being measured by a planar RPA. In addition to the spreading, there is also a significant amount of current collected when the retarding potential is greater than the extraction potential. This can be attributed to the coarseness of the grids. A coarse grid will have some potential sagging, meaning that the potential in the openings will not be uniform which would allow for ions of lower energies to pass through.

In order to confirm that features in the plot shown can be attributed to the effects of a planar RPA, a simple analysis can be performed. Consider an axisymmetric ion beam with angular current distribution f_θ and an energy distribution f_E that is the same along any path (i.e., assume the energy distribution is independent of the angle). The current passing through an aperture that has an acceptance angle of α_0 will be given by

$$I_c = \int_0^{\alpha_0} f(\theta) \sin \theta d\theta \quad (5.4)$$

within a normalization constant. When using an RPA, ideally the current collected

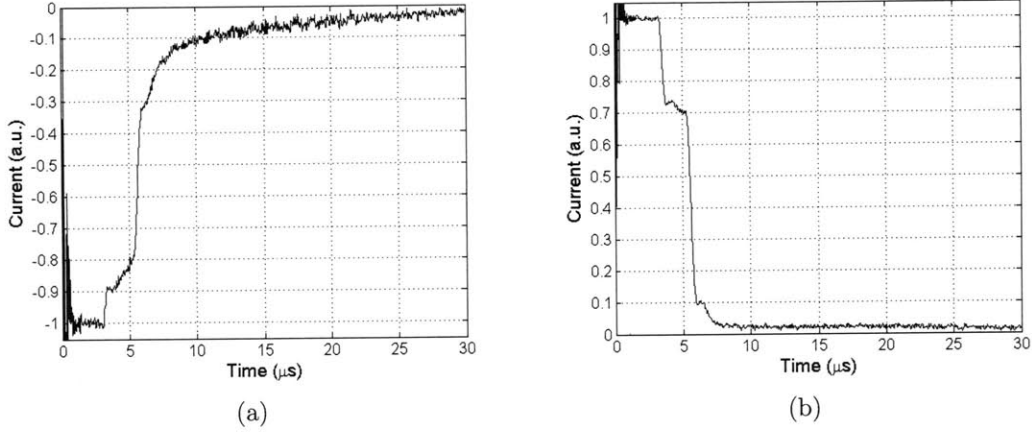


Figure 5-7: Full beam TOF signals for an EMI-BF₄ ILIS operating at (a)-2000V and (b) 2250V

will be simply given by integrating the energy distribution,

$$I_c = \int_{\phi_{RPA}}^{\infty} f(\phi) d\phi \quad (5.5)$$

However, in light of the effects of beam divergence contained in Eq. 5.3, the previous two equations do not hold. Instead, a combination of the two must be used, so that the collected current is actually

$$I_c(\phi_{RPA}) = \int_0^{\alpha_0} \int_{\frac{\phi_{RPA}}{\cos^2 \theta}}^{\infty} f(\phi) f(\theta) \sin \theta d\phi d\theta. \quad (5.6)$$

The effects of this beam spreading can be seen best by plotting Eq. 5.6. Consider an EMI-BF₄ ILIS operating at $\phi_a = -1650\text{V}$. Based on the results discussed in this paper, the energy distribution is expected to have a narrow peak just below 1650eV, a broader, smaller peak at $\frac{m_0}{m_1}\phi_a = 503\text{eV}$, and a slight offset from zero in between the peaks. This energy distribution, shown in Fig. 5-10, is idealized as being the superposition of two gaussian functions and a step function. The main energy peak is defined to have a FWHM of 10eV, and an area under its curve of 0.47. The secondary peak has a FWHM of 100 eV, and an area of 0.28. The step function has an area of 0.25, and spans from 503eV to 1650eV.

The angular distribution function can be assumed to be quadratic, with a half

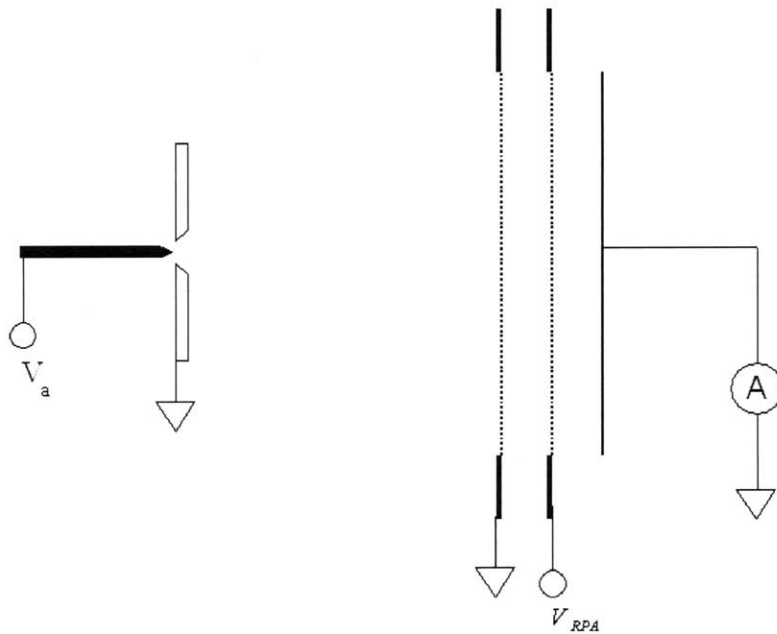


Figure 5-8: Schematic of the full beam RPA assembly

angle of approximately 20° , as discussed in Sec. 2.2.1. Under these assumptions, the RPA output (with current normalized to have a maximum of unity), is shown in Fig. 5-11. In addition to the idealized RPA output are the estimated effects of the beam divergence from Eq. 5.6, as well an actual experimental result. The beam spreading seems to have the most dramatic effect at energies near the beam energy, where a sharp drop off in current is expected. The broader step due to the ion fragmentation at 503eV and the linear slope region are hardly changed at all. The calculated effect of the beam spreading is seen to agree well with what was observed in the experiment, indicating that the ILIS used likely had parameters similar to those used for the simulation.

It is of note that the non-ideal calculation and experimental curves both show the presence of current at energies greater than 1650eV. This is attributed to the coarseness of the grid, which allows ions of lower energy to pass through. This effect was taken into account by assuming that the grid potential sagged up to 10% and the amount of current of lower energies passing through decreases linearly, i.e., when the RPA voltage is ϕ_{RPA} , all the ions with energies lower than $0.9\phi_{RPA}$ are stopped, while

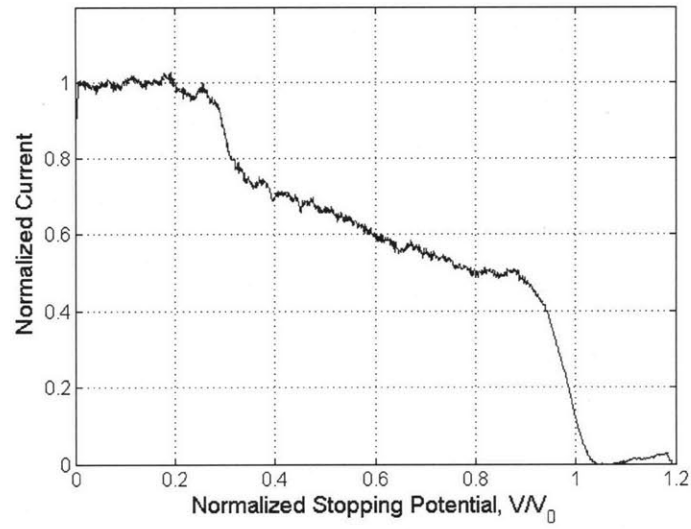


Figure 5-9: Output of the full beam RPA with an EMI-BF₄ ILIS operating at -1650V
all those with energies greater than ϕ_{RPA} are allowed to pass, with linear behavior in
between.

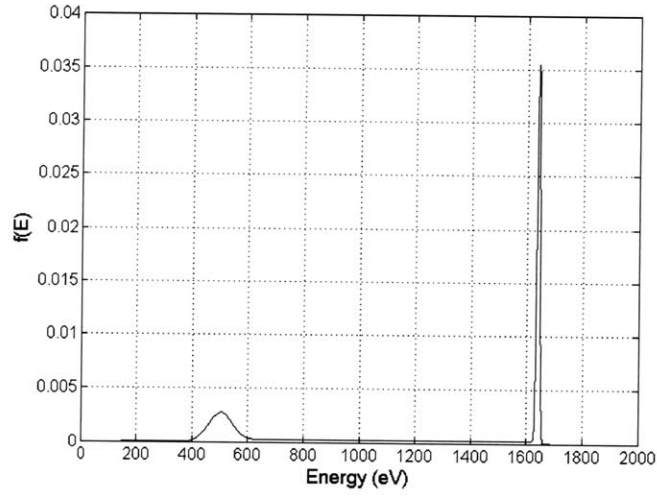


Figure 5-10: Idealized energy distribution for an EMI-BF₄ ILIS

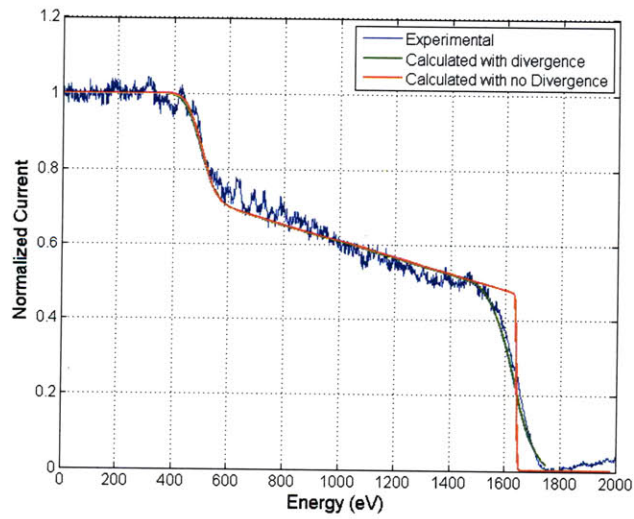


Figure 5-11: Effect of beam divergence on an RPA current signal for an EMI-BF₄ ILIS

Chapter 6

Ion Fragmentation

As briefly mentioned in prior sections, there are signs that the solvated ions extracted from an ILIS can fragment into a neutral particle and an ion with a lower degree of solvation. The occurrence of this breakup in the field free post-acceleration region has been seen in previous studies of ILIS [16]. However, there are also signs that there is a significant amount of ion fragmentation occurring in the acceleration region between the emitter and extractor electrodes. This chapter contains a discussion of these signs, as well as the implications of this fragmentation for ILIS applications.

6.1 Signs of Fragmented Ions

As briefly mentioned in Ch. 5, the signs of ion fragmentation occur in the data obtained from the RPA instrument. For example, consider the RPA current signal obtained from a BMI-I ILIS operating at -1.5kV shown in Fig. 6-1.

The labeled peaks in the figure indicate the presence of ion populations characterized by discrete energies with a finite spread. The larger peak is the primary population of ion species, being composed of those non-solvated and solvated ions ($n = 0,1,2$) that are accelerated through the full applied potential. The smaller peaks are the result of ion breakup after the acceleration region, as described by Eq. 3.5. However, consider a solvated ion with $n = a$ that fragments into a neutral and an ion with $n = b$ ($0 < b < a$) in the acceleration region, where the local potential, ϕ_f , is

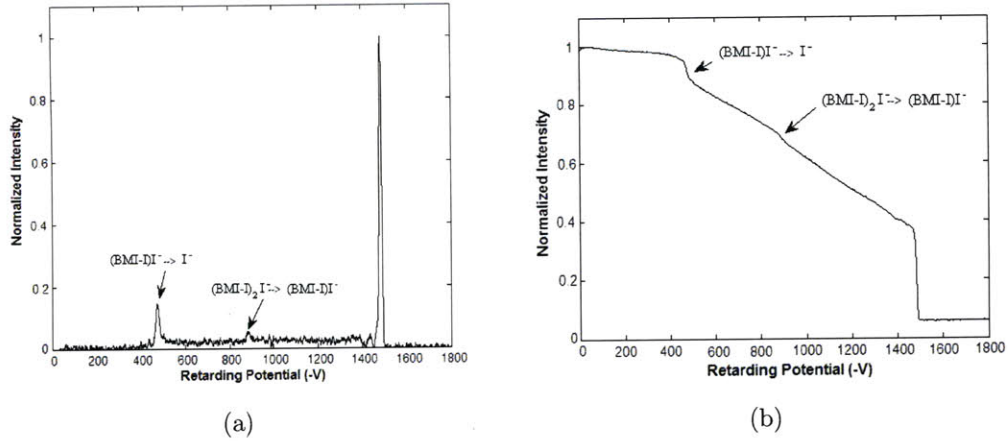


Figure 6-1: RPA energy spectrum and current signal for a BMI-I ILIS operating at -1.5kV

$0 < |\phi_f| < |\phi_a|$. The stopping potential for the fragmented ion will be

$$\phi_s = \frac{m_b}{m_a}(\phi_a - \phi_f) + \phi_f. \quad (6.1)$$

The minimum value of the stopping potential given by Eq. 6.1 occurs when fragmentation takes place in a region where $\phi_f = 0$, i.e., after the acceleration region. The maximum value occurs when fragmentation takes place when ϕ_f is very near to ϕ_a , i.e., immediately after emission. Therefore the stopping potentials will be contained within

$$\frac{m_b}{m_a}\phi_a < \phi_s < \phi_a \quad (6.2)$$

which is precisely what is seen in the RPA output in Fig. 4-5, for the case of $a = 1$ and $b = 0$ for a BMI-I ILIS. It is this well defined containment of the secondary signal within the ranges established by Eq. 6.2 that suggests that there is significant amounts of ion fragmentation occurring within the acceleration region.

6.2 Causes

Although the data collected for this thesis is not substantial enough to develop a theory as to the mechanics of this ion fragmentation, there are several possibilities that can guide future experiments. It is obvious from the gathered data that the emitted solvated ions are at least metastable, as some of them can survive long enough to fragment after the acceleration region, while some will fragment within it. Initial guesses for why this fragmentation is occurring can be divided into two categories, either collisions or from internal energy.

6.2.1 Collisions

Two types of collision are possible causes for fragmentation of the solvated ions, either collisions with background neutrals, or with the faster moving non-solvated ions. It is highly unlikely that collisions with background neutrals have a significant effect, as the operation pressure is so low. This leaves the option of ion-ion collisions. As an initial check for this, the mean free path of the ions can be calculated to see if collisions are very likely. The interaction of the non solvated ions with the singly solvated ions in the acceleration can be characterized by the coulomb cross section [1],

$$\sigma_t = \pi b_0^2 \left[\frac{1}{\sin^2(\chi_{min}/2)} - 1 \right] \quad (6.3)$$

where χ is the scattering angle and b_0 is

$$b_0 = \frac{q^2}{4\pi\epsilon_0\mu g^2}. \quad (6.4)$$

In the definition of b_0 , μ is the reduced mass and g is the relative velocity between the two ion species.

$$\mu = \frac{m_0 m_1}{m_0 + m_1} \quad (6.5)$$

The mean free path is calculated from

$$\lambda_{mfp} = \frac{1}{n\sigma} \quad (6.6)$$

For an ILIS, the number density of particles can be approximated from the total current, the beam divergence, and an estimated source size. The current density can be approximated as the total current divided by the area of the spherical cap defined by the beam half-angle. Then the number density of particles can be obtained from $qnv = J$, or

$$n = \frac{I}{qv} \frac{1}{2\pi R^2(1 - \cos \theta_0)} \quad (6.7)$$

The velocities in Eqs. 6.7 and 6.4 can be obtained from the potential distribution. For this analysis, a simple model was created in COMSOL Multiphysics to obtain the potential distribution along the axis of a tip with a radius of curvature of about 50 μm . Then the mean free path is obtained using Eq. 6.6. The results of this analysis are shown in Fig. 6-2

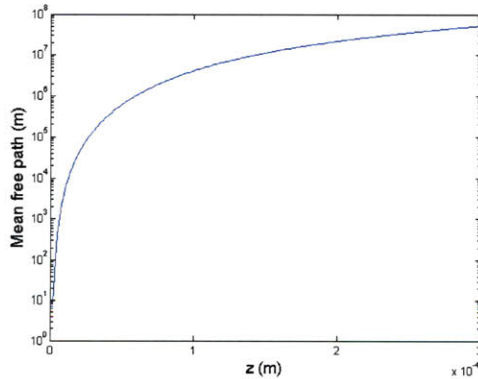


Figure 6-2: Mean free path of non-solvated ions in an EMI-BF₄ ILIS at 1500V

As can be seen in the figure, the mean free path quickly grows to orders of magnitude greater than the size of the device itself. This means that any collisions that do occur, must happen immediately after the emission. Thus, collisions in the acceleration region cannot explain the continuous distribution of fragmentation that is observed.

6.2.2 Internal Energy

Another possible cause of the ion fragmentation due to molecular vibrations caused by internal energy. Possible sources of this energy are thermal energy or from the extraction process. The thermal energy would be given by the normal $k_B T$, which gives energies much less than 1 eV for normal ILIS operating conditions. These low energies don't seem likely to be the cause of fragmentation, but it is something that can be investigated. Another possibility is that the extraction process deposits some energy into the molecule. When ions are extracted from an ILIS, there have been seen to be energy deficits greater than 5 eV [16, 14]. It has been assumed previously that this lost energy went into heating of the source itself, but it may be possible that a portion of this energy is transferred to the extracted ions, which may provide enough energy for ion fragmentation. It should be noted that these are very first guesses as to what is causing the ion fragmentation, and should merely serve to provide some guidance for future studies.

6.3 Effects of Ion Fragmentation

6.3.1 Performance of an ILIS Based Thruster

The previously documented fragmentation of ions in the post-acceleration region has negligible impact on the performance of an ILIS thruster. This is because the pre-breakup ion has already undergone its full acceleration, and already left the thruster. If the fragmentation occurs in the acceleration regions, however, the resulting ion will continue to accelerate but the neutral will travel at a constant speed, resulting in lower performance as compared to fragmentation after it had obtained its highest possible velocity. An important distinction to note here is that while all plasma-based electric propulsion devices have inefficiencies due to neutrals escaping. However, in other thruster the neutrals leave with only their thermal velocity, having a negligible contribution to thrust, while in the ILIS thruster, the neutrals are energetic, still contributing to the total thrust.

In order to characterize the effect of ion fragmentation on the efficiency of an ILIS thruster, a modification can be made to the polydispersive efficiency as defined in Eq. 2.9. In addition to the discrete ion populations of different degrees of solvation n , there will also be a population of ions and neutrals that have a certain distribution of energies. Based on the RPA data shown in Fig. 4-5, there appears to be a linear energy distribution of the ion fragmentation products. To simplify the analysis, characterize the fragmented ion population by the energy it would have if all fragmentation occurred halfway through the acceleration region, at a potential $\phi_a/2$. Eq. 6.1 can be used to determine the energy and corresponding particle velocity,

$$\frac{1}{2}m_0v^2 = q \left(\frac{m_0}{m_1} + 1 \right) \frac{\phi_a}{2} \quad (6.8)$$

$$c_f = c_0 \sqrt{\frac{1}{2} \left(\frac{m_0}{m_1} + 1 \right)} \quad (6.9)$$

where c_0 is the velocity of the full accelerated non-solvated ion, given by

$$c_0 = \sqrt{2 \frac{q}{m} \phi_a}. \quad (6.10)$$

In addition to the population of fragmented ions, there will be a conjugate population of energetic neutrals which maintain the same speed they had at fragmentation,

$$c_n = c_0 \sqrt{\frac{\zeta}{2}}. \quad (6.11)$$

The new populations of fragmentation products can be integrated into the definition of polydispersive efficiency, yielding the expression

$$\eta_p = \frac{\frac{1}{2} \left[\sqrt{2\zeta} f_0 + \sqrt{2} f_1 + \left(\sqrt{\zeta \left(1 + \frac{m_0}{m_1} \right) + \frac{m_n}{m_1}} \right) f_f \right]^2}{\zeta f_0 + f_1 + \left(\zeta + \frac{m_n}{m_1} \right) f_f}. \quad (6.12)$$

The impact of the fragmentation on the efficiency of an ILIS thruster can be seen by plotting Eq. 6.12 for several different parameters. For example, consider an EMI-BF₄ ILIS operating in the positive mode. The majority of the beam emitted by such

a source will be composed of non-solvated and singly-solvated ions, allowing for the application of Eq. 6.12. The ion masses are 111.2 amu and 309.2 amu for EMI^+ and $(\text{EMI-BF}_4)\text{EMI}^+$, respectively, giving a value of 2.78 for the specific charge ratio, ζ . The mass of the neutral particle, EMI-BF_4 , is 198 amu. The modified polydispersive efficiency for these conditions is plotted in Fig. 6-3.

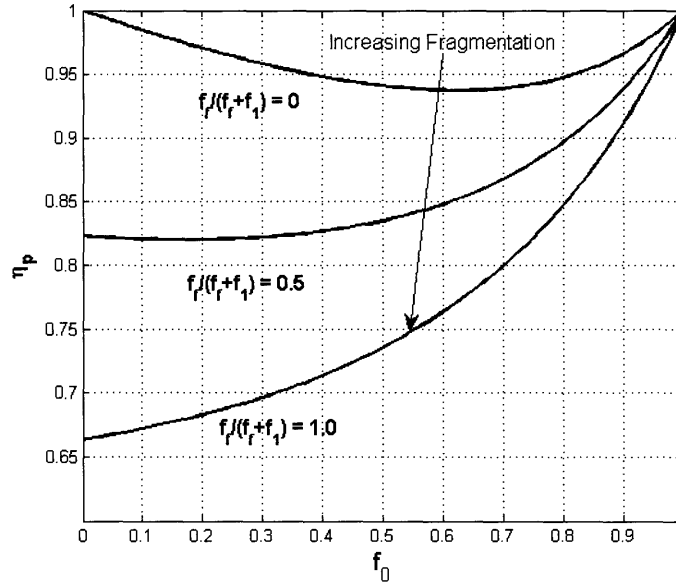


Figure 6-3: Effect of ion fragmentation on the polydispersive efficiency for an EMI-BF_4 ILIS operating in the positive mode

The amount of fragmentation is represented in the figure is characterized by the quantity $f_f/(f_f + f_1)$. For a fixed portion of non-solvated ions, given by f_0 , this quantity represents the remaining portion of the beam composed of fragmentation products. In other words, it is the portion of the emitted $n = 1$ solvated ions that fragment in the acceleration region. The general trend is for increasing amounts of fragmentation to decrease the efficiency. The worst case scenario is a drop from $\eta_p \approx 1$ to $\eta_p \approx 0.66$, in the case in which only singly solvated ions are emitted, all of which fragment while accelerating. A more reasonable case, however, is in which one quarter of the beam is composed of non-solvated ions ($f_0 = 0.25$), and the fragmentation products compose 25% of the beam ($f_f = 0.25$, $f_1 = 0.5$), as seen in the RPA output in Fig. 5-9. In this case, the polydispersive efficiency is approximately $\eta_p \approx 0.88$,

whereas for $f_0 = 0.25$ and $f_1 = 0.75$ it would have been $\eta_p \approx 0.94$. This shows that ion fragmentation in the region between the emitter and extractor in an ILIS thruster has a significant effect on efficiency, being in the range of about 6% in this example.

6.3.2 FIB

When being used in a FIB system, the secondary population of ions produced by the ion fragmentation would likely be scattered by the focusing optics and intercepted by the apertures. The neutral population, however, might be a significant issue. The neutrals will continue on straight line trajectories, possibly impacting the target sample, which may be a problem. Of particular concern would be operating the BMI-I ILIS in the negative mode with the intention for the production of a pure I^- beam. Mass filtering could be used to remove the solvated ions, but the neutrals would continue on their trajectories. The simplest solution to this issue is the addition of a curved magnetic sector, which would bend the trajectories of the iodine ions, but not the neutrals. This solution is adequate for a newly designed FIB system, but may not be an easy solution when integrating the BMI-I ILIS into an existing instrument.

Chapter 7

Conclusions and Future Work

7.1 BMI-I ILIS

This initial work on the BMI-I ILIS is promising. An ion beam composed of nearly 50% pure iodine has been produced, and shown to have energy characteristics that are not greatly different than other ILIS. An initial estimate predicts that performance of this source in a FIB column will be significantly less than that of the traditionally used LMIS, but possibly still within a useful range. Specifically, beam currents of >100 nA were obtained, with energy deficits of approximately 9-15 eV and FWHM of 12 eV. More characterization and refinement of the source needs to be performed before it may be useful in an actual FIB system. The angular intensity approximation needs to be confirmed, by direct measurement of the angular current distribution or some other method. Spot size measurements, perhaps those described by Zorzos and Lozano [24], need to be performed to verify these initial estimates. In addition to more characterization, the applications for such an ion source need more investigation. Specifically, etching rates need to be established, particularly for GaAs and other materials of interest.

7.2 Ion Fragmentation

The presence of ion fragmentation in the acceleration region of an ILIS is seen to have significant impacts on applications in propulsion and FIB. The efficiency of an ILIS thruster is reduced significantly by such fragmentation, while the use of such a source in a FIB column would require special consideration. Further scientific studies need to be performed in order to ascertain the physics behind the fragmentation. Specifically, it is currently unclear as to why this fragmentation occurs. Several guesses as to the mechanisms behind the fragmentation were discussed in Sec. 6.2, but none were completely ruled out. Specific experiments are planned to determine the rate of ion fragmentation in the field-free region. By mounting an RPA on a linear stage, and varying the distance between the ILIS and the instrument, changes in the amount of fragmentation due to a longer flight time will be measurable. Also planned are experiments dealing with the temperature effect on fragmentation rates and ratios.

Appendix A

Drawings of the Full Beam Time of Flight Assembly

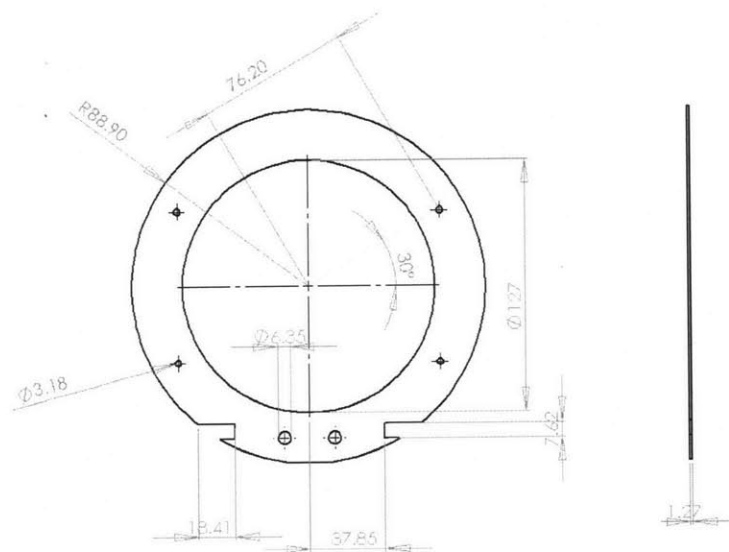


Figure A-1: Full beam TOF front plate

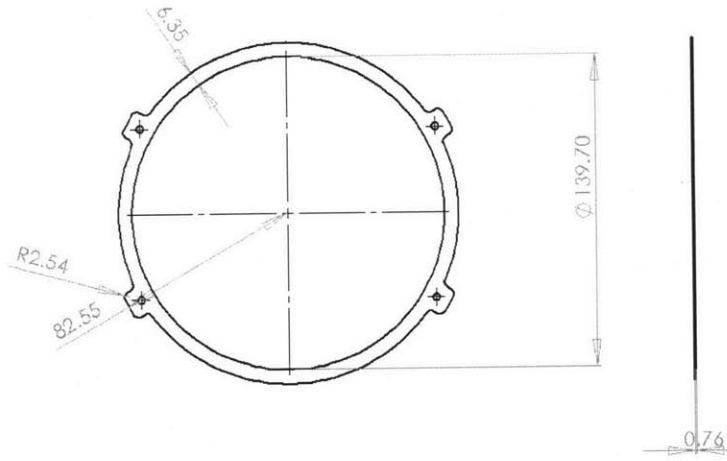


Figure A-2: Full beam TOF secondary electron grid

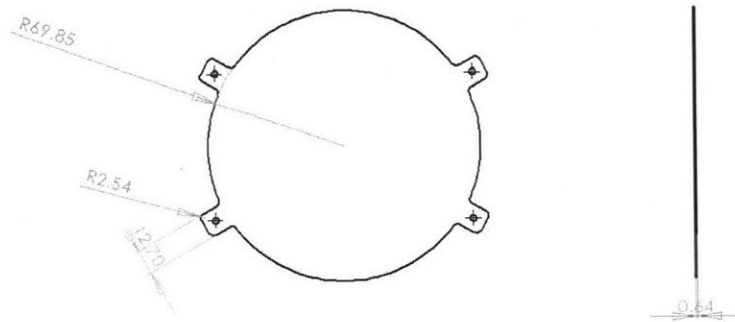


Figure A-3: Full beam TOF collector

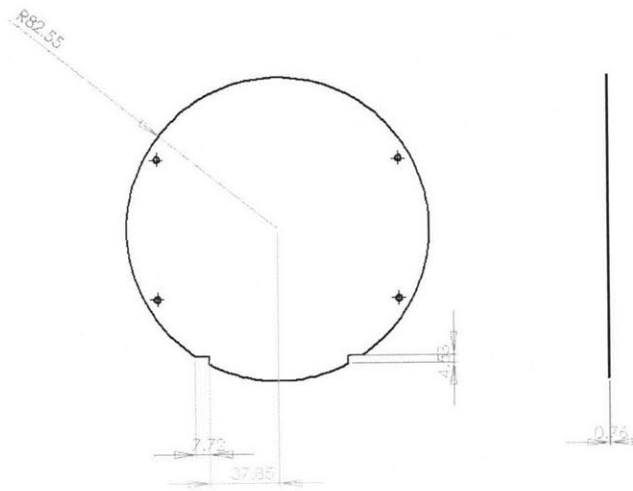


Figure A-4: Full beam TOF back plate

Bibliography

- [1] J.A. Bittencourt. *Fundamentals of Plasma Physics*. Springer, New York, third edition, 2004.
- [2] Michel Cloupeau and Bernard Prunet-Foch. Electrohydrodynamic spraying functioning modes: a critical review. *Journal of Aerosol Science*, 25(6):1021–1036, 1994.
- [3] Daniel G. Courtney, Hanqing Li, Pablo Diaz Gomez Maqueo, Timothy P. Fedkiw, and Paulo C. Lozano. On the validation of porous nickel as substrate material for electrospray ion propulsion. In *46th AIAA/ASME/SAE/ASEE Joint Propulsion Conference and Exhibit*.
- [4] Daniel G. Courtney and Paulo C. Lozano. Porous ionic liquid ion source fabrication refinements and variable beam energy experiments. In *45th AIAA/ASME/SAE/ASEE Joint Propulsion Conference and Exhibit*, Denver, CO, August 2009.
- [5] Jones de Andrade, Elvis S. Böes, and Hubert Stassen. Computational study of room temperature molten salts composed by 1-alkyl-3-methylimidazolium cations - force-field proposal and validation. *Journal of Physical Chemistry B*, 106:13344–13351, 2002.
- [6] J. Fernaández de la Mora and I. G. Loscertales. The current emitted by highly conducting taylor cones. *Journal of Fluid Mechanics*, 260:155–184, 1994.
- [7] Juan Fernández de la Mora. The fluid dynamics of taylor cones. *Annual Review Fluid Mechanics*, 39:217–243, 2007.
- [8] M. Gamero-Castaño and V. Hruby. Electrospray as a source of nanoparticles for efficient colloid thrusters. *Journal of Propulsion and Power*, 17(5):977–986, 2001.
- [9] Jacques Gierak. Focused ion beam technology and ultimate applications. *Semiconductor Science and Technology*, 24:217–243, 2009.
- [10] F. J. Higuera. Model of the meniscus of an ionic-liquid ion source. *Physical Review E*, 77(026308), 2008.

- [11] Y.L.D. Ho, R. Gibson, C. Y. Hu, M. J. Cryan, J. G. Rarity, P. J. Heard, J. A. Timpson, A. M. Fox, M. S. Skolnick, M. Hopkinson, and A. Tahraoui. Focused ion beam etching for the fabrication of micropillar microcavities made of iii-v semiconductor materials. *Journal of Vacuum Science and Technology B*, 25(4):1197–1202, 2007.
- [12] Robert S. Legge. Fabrication and characterization of porous metal emitters for electrospray applications. Master’s project, Massachusetts Institute of Technology, Department of Aeronautics and Astronautics, June 2008.
- [13] Paulo Lozano and Manuel Martinez-Sanchez. Efficiency estimation of emi- bf_4 ionic liquid electrospray thruster. In *41st AIAA/ASME/SAE/ASEE Joint Propulsion Conference and Exhibit*, Tucson, AZ, July 2005.
- [14] Paulo Lozano and Manuel Martínez-Sánchez. Ionic liquid ion sources: characterization of externally wetted emitters. *Journal of Colloid and Interface Science*, 282:415–421, 2005.
- [15] Paulo C. Lozano. *Studies on the Ion-Droplet Mixed Regime in Colloid Thrusters*. PhD dissertation, Massachusetts Institute of Technology, Department of Aeronautics and Astronautics, February 2003.
- [16] Paulo C. Lozano. Energy properties of an emi-im ionic liquid ion source. *Journal of Physics D: Applied Physics*, 39:126–134, 2006.
- [17] Jon Orloff, Mark Utlaut, and Lynwood Swanson. *High Resolution Focused Ion Beams*. Kluwer Academic/Plenum Publishers, New York, 2003.
- [18] Carla Perez-Martinez, Stéphane Guilet, Noëlle Gogneau, Pascale Jegou, Jacques Gierak, and Paulo Lozano. Development of ion sources from ionic liquids for microfabrication. *Journal of Vacuum Science and Technology B*, 28(3), 2010.
- [19] I. Romero-Sanz, R. Bocanegra, J. Fernandez de la Mora, and M. Gamero-Castaño. Source of heavy molecular ions based on taylor cones of ionic liquids operating in the pure ion evaporation regime. *Journal of Applied Physics*, 94(5):3599–3605, 2003.
- [20] P. Lozano S. Sümer and M. Martinez-Sanchez. Characterization of a variable isp ionic liquid electrospray thruster beam. In *42nd AIAA/ASME/SAE/ASEE Joint Propulsion Conference and Exhibit*, Sacramento, CA, July 2006.
- [21] G.I. Taylor. Disintegration of water drops in an electric field. *Proceedings of the Royal Society of London*, (280), 1964.
- [22] J. Zhou, W. Ens, and K.G. Standing. A dual ion source to produce cs^+ or i^- ions for secondary ion mass spectrometry. *International Journal of Mass Spectrometry and Ion Processes*, 146, 1995.

- [23] Anthony N. Zorzos. The use of ionic liquid ion sources (ilis) in fib. Master's project, Massachusetts Institute of Technology, Department of Aeronautics and Astronautics, August 2009.
- [24] Anthony N. Zorzos and Paulo C. Lozano. The use of ionic liquid ion sources in focused ion beam applications. *Journal of Vacuum Science and Technology B*, 26(6):2097–2102, 2008.
- [25] Y. Zou, Y. Cui, V. Yun, A. Valfells, R.A. Kishek, S. Bernal, I. Haber, M. Reiser, P.G. O'Shea, and J.G. Wang. Compact high-resolution retarding field analyzer for space-charge-dominated electron beams. *Physical Review Special Topics - Accelerators and Beams*, 5(072801), 2002.